Summer 2015

# Modelling of interconnects in 3DIC based on layered green functions

Siming Pan



Department: Electrical and Computer Engineering

# MODELLING OF INTERCONNECTS IN 3DIC BASED ON LAYERED GREEN FUNCTIONS

by

SIMING PAN

A DISSERTATION

Presented to the Faculty of the Graduate School of the

MISSOURI UNIVERSITY OF SCIENCE AND TECHNOLOGY

In Partial Fulfillment of the Requirements for the Degree

DOCTOR OF PHILOSOPHY

in

ELECTRICAL ENGINEERING

2015

Approved by

Dr. Jun Fan
Dr. Yaojiang Zhang
Dr. James Drewniak
Dr. David Pommerenke
Dr. Matt O'Keefe

## PUBLICATION DISSERTATION OPTION

This dissertation has been prepared in the style utilized by the Journal of IEEE (Institute of Electrical and Electronics Engineers) Transactions on Electromagnetic Capability, listed as follows:

Paper 1, S. Pan, J. Fan, “GREEN'S FUNCTION FOR PLANAR SI-SIO2 MEDIA”, to be submitted to IEEE Trans. on EMC., 2015.

Paper 2, S. Pan, J. Fan, “An Efficient Method to Extract Surface-Wave Poles of Green’s Functions near Branch Cut in Lossy Layered Media”, published on Antennas and Propagation, IEEE Transactions on

Paper 3, S. Pan, J. Fan, “Modeling of Coplanar Waveguide on 2.5D Silicon Interposer”, to be submitted to IEEE Trans. on EMC., 2015.

# ABSTRACT

As traditional CMOS scaling pace gradually slows down, three-dimensional (3D) integration offers another dimension of in the ”More-than-Moore” era. In this dissertation, a number of investigations were conducted to better model interconnects in 3D integrated circuit (IC), to evaluate electrical behavior including delay, power consumption, signal integrity (SI), and power integrity (PI) for 3D ICs. Partial Element Equivalent Circuit (PEEC) method with layered Green’s function is studied here, since it consumes less computational resources and provides better physical insight to model the interconnects in 3DIC for high-speed digital circuits. The work is organized as a series of papers. The first paper reviewed the fundamental methods to derive layered Green’s function in spectral domain using discrete complex image method (DCIM) and analyzed the effects of each Green function terms to model silicon interconnects. The second paper proposed a unique method to extract poles near branch cut in complex kp plane, to accurately extract surface wave effects. The last paper proposed a new equivalent circuit model for coplanar waveguide (CPW) structure on 3DIC. The silicon effects on series inductance were also studied by employing the modified Green functions with semiconductor images at a complex distance from spectral-domain analysis.

# ACKNOWLEDGMENTS

I would like to express my sincere gratitude to Dr. Jun Fan, my advisor, for his guidance and instruction on my research work, financial support to my study and direction for this dissertation during my pursuit of the PhD's degree. I learned not only academic knowledge from Dr. Jun Fan, but also the rigorous attitude, good manners, and courage to face difficulties.

I would like to thank Dr. Daryl Beetner, Dr. David J. Pommerenke, Dr. Victor Khilkevich and Dr. James Drewniak, for their teaching in my courses, discussions related to my research and helpful suggestions on my dissertation.

I would also like to express my thanks to all the other faculty members and students in and out of the EMC lab for their team work and help in my coursework and research.

Finally, I would like to thank my family for their endless love and endless support in my life.

# TABLE OF CONTENTS

Page

# LIST OF ILLUSTRATIONS

Figure Page

PAPER I

PAPER II



PAPER III

# LIST OF TABLES

# 1. INTRODUCTION

As traditional CMOS scaling pace gradually slows down, three-dimensional (3D) integration offers another dimension of in the ”More-than-Moore” era. In this dissertation, a number of investigations were conducted to better model interconnects in 3D integrated circuit (IC), to evaluate electrical behavior including delay, power consumption, signal integrity (SI), and power integrity (PI) for 3D ICs. Partial Element Equivalent Circuit (PEEC) method with layered Green’s function is studied here, since it consumes less computational resources and provides better physical insight to model the interconnects in 3DIC for high-speed digital circuits.

The work is organized as a series of papers. The first paper reviewed the fundamental methods to derive layered Green’s function in spectral domain using discrete complex image method (DCIM) and analyzed the effects of each Green function terms to model silicon interconnects. The second paper proposed a unique method to extract poles near branch cut in complex kp plane, to accurately extract surface wave effects. The last paper proposed a new equivalent circuit model for coplanar waveguide (CPW) structure on 3DIC. The silicon effects on series inductance were also studied by employing the modified Green functions with semiconductor images at a complex distance from spectral-domain analysis.

In the first paper, previous method of deriving Green function in multi-layer media was reviewed. DCIM has been used to derive the Green function with lossy media. The study of applying the methods to the real applications of 3DIC shows at image theories can be applied to magnetic vector Green functions at low frequency, however, multiple images should be considered for electric potential Green’s function. At high

frequency, surface-wave term has far-field effects when the distance of the interconnect is far. Spatial-wave term becomes to dominate when the pitch size becomes larger.

In the second paper, a robust and automatic method to extract the surface-wave poles of the spectral-domain Green's functions for general layered media is proposed. Both lossless and lossy dielectric materials can be effectively handled. The proposed method can accurately identify the surface-wave poles located close to the branch cut. Through the numerical examples and the comparisons with the previously published results, the proposed approach has been demonstrated more effective and accurate to handle lossy layered media.

In the third paper, a new equivalent circuit model is proposed to model coplanar traces on silicon interposer was proposed. The 2D lossy metal-isolator-semiconductor (MIS) coplanar waveguide (CPW) is represented by simple RLGC circuit derived based on PEEC method. The model provides physical insight and directly related to geometry. It is also demonstrated in the paper that the silicon effects on series impedance can be neglected in conventional CMOS processes. A test 2.5 silicon interposer is fabricated to validate the effectiveness of the model. The presented circuit model shows good correlations with full-wave simulations as well as the measurements on the test interposer.

The primary contributions of this dissertation include:

- Equivalent Transition Line Model for Via Structures.
- Radiated and Conductive Emission Models for Integrated Circuit.
- Passivity and Causality Analysis in the Link Path.
- Power Distribution Network Design and Optimization.

- Modelling of TSV arrays by extension of PEEC methods.
- A Technique to Accelerate Computational Efficiency for PEEC
- Derivation of Green's Function in Multi-Layered Media
- A Pole Extraction Method to Handle Branch Cut
- Modelling of On-Silicon Coplanar Waveguide with Homogenous Decomposition
- Modelling Guidelines for interconnects on 2.5D interposer and 3DIC

## PAPER

# I. GREEN'S FUNCTION FOR PLANAR SI-SIO2 MEDIA

Siming Pan, *Student Member, IEEE*

***Abstract*—**As traditional CMOS scaling pace gradually slows down, three-dimensional (3D) integration offers another dimension of in the ”More-than-Moore” era. This paper reviewed the fundamental methods to derive layered Green’s function in spectral domain using discrete complex image method (DCIM) and analyzed the effects of each Green function terms to model silicon interconnects. Firstly we derived the general form of spectral domain Green’s function for multilayer media based on transmission line analogy and generalized reflection/transmission coefficients for potentials. Then, DCIM techniques are used to evaluate Sommerfeld integration for spatial domain Green’s functions. Specifically, equivalent partial circuit elements for various on-chip interconnects are discussed based on the properties of the Green’s functions due to different modes and material of semiconductor.

*Index Terms*—Green’s functions, surface-wave poles, planar si-sio2 media, pole extraction, Sommerfeld integral.

## I. INTRODUCTION

Green’s function is the solution to the partial differential equation with a unit source subject to specific initial conditions or boundary conditions. It is similar to the impulse response in a linear system. The solution of the actual driving function could be

derived through a superposition of the Green's function with the Dirac delta source at different locations [1]~[3]. PEEC formulations require extended solutions of integral equations, in which evaluation of Green's functions are critical to obtain an efficient and accurate solution of circuit model. A critical step in the formulation involves the calculation of the reaction integrals to construct MoM matrix, both in the spectral domain [4], [5] and in the spatial domain [6]~-[8].

In the layered media, the spectral-domain dyadic Green's functions (DGF) are easier to obtain through one-dimensional generalized reflection and transmission [12] or transmission line analogy [13]. It may be directly used in the integral-equation formulations based on spectral domain approach (SDA) [14-16]. However, the SDA requires double spectral integrals, which could be transformed to Sommerfeld integrals in the spatial domain [17].

To evaluate Sommerfeld integrals has been studied extensively in the previous work. As the kernel of the Sommerfeld integral is general oscillatory and contains singularities with the slowly-decaying parts in the complex kp plane, the direct numerical integration is time-consuming. The most popular methods to accelerate the calculations of Sommerfeld integration include the steepest-descent path (SDP) approach [18], [19] , pole-residue representation approach [5], [20], fast Hankel transform technique [21], the window function approach [22] and the discrete complex image method (DCIM) [23]-[27].We mainly discuss the development Green's function for planar Si-Sio2 media based on DCIM approach. The basic idea of DCIM is to approximate the kernel of the spectral-domain Sommerfeld integral with summation of complex exponentials, so that closed-from solutions can be derived using Sommerfeld identity. This method is initially

proposed by Y Chow in [23], where he firstly extracted the quasi-static image (which contributes in the near-field region) and surface-wave terms (which contributes in the far-field region) from the kernel. Then prony's method was applied to transform the remaining portion to complex exponentials. The improved Prony method was proposed in [24] with least-square techniques for complex images. But both methods require error iterations, which make them inefficient and less robust. Generalized pencil of functions (GPOF) was employed in [25] and [26] to replace prony's methods. However, even with surface extracted, errors occur in the near-field region due to the primary singularity at the origin for Hankel functions when $z \neq z'$. Without surface wave extracted, errors occur in the far-field region because it is physically inappropriate to approximate the cylindrical surface waves by spherical waves (complex images) [4]. Recently, a direct discrete complex image method was proposed in [27], where the authors selected a novel integration path to avoid wave extractions. But this method is not computationally efficient.

In the applications of modern on-chip interconnects design, especially for the newly emerging 3D integration, the modeling of 3-D interconnects involves inhomogeneous metal-isolation-silicon (MIS) environment. Typically, the vertical Si-Sio2 layered media could affect the performance of interconnects for high-speed applications. However, in the previous work, quasi-static approximation with free-space Green's function is generally used in the on-chip interconnect design [9], [10]. Until very recently, it is safe in many cases to solve sparse, electrically small problems using quasi-static methods. By definition, electrically small in frequency domain means

$$d_{\max} \leq 30/(nf_{\max}) \tag{1}$$

where $d_{\max}$ is the maximum dimension, $f_{\max}$ is the maximum frequency and n is a number between 10 and 20.

In time domain, the definition for electrically small generally becomes

$$d_{\max} < \frac{1}{n\tau} \tag{2}$$

where $\tau$ is the rise or fall time of the digital signal.

Nevertheless, with bandwidth continuing to grow to meet the needs of switch, server and storage consolidation, data center development and processor communication [11], the on-chip signal link modeling cannot be considered as electrically small. Thus, it could loss great accuracy for high-frequency analysis without evaluation of Green's function for Si-Sio2 media.

In this work, firstly we derived the general form of spectral domain Green's function for multilayer media based on transmission line analogy and generalized reflection/transmission coefficients for potentials. Then, DCIM techniques are used to evaluate Sommerfeld intergration for spatial domain Green's functions. Specificlly, equivalent patial circuit elements for various on-chip interconnects are discussed based on the properties of the Green's functions due to different modes and material of semiconductor.

## II. SPECTRAL-DOMAIN GREEN'S FUNCTION

Consider a general multilayer medium with a point source $(\mathbf{J}, \mathbf{M})$ embeded in layer i, as shown in Fig. 1. The fields $(\mathbf{E}, \mathbf{H})$ due to the point source are governed by the Maxwell's equations

$$\nabla \times \mathbf{E} = -j\omega\mu_0\mu_r\mathbf{H} - \mathbf{M}$$
$$\nabla \times \mathbf{H} = j\omega\varepsilon_0\varepsilon_r\mathbf{E} + \mathbf{J} \tag{3}$$

For layered medium, since the medium is infinite large in the (x,y) plane, spectral-domain analysis are commonly used to transfer the transvese coodinate $\boldsymbol{\rho} = \hat{\mathbf{x}}x + \hat{\mathbf{y}}y$ to its spectral counterpart $\mathbf{k}_\rho = \hat{\mathbf{x}}k_x + \hat{\mathbf{y}}k_y$ by the Fourier transform pair

$$F[f(\mathbf{r})] \equiv \tilde{f}(\mathbf{k}_\rho; z) = \int_{-\infty-\infty}^{+\infty+\infty} f(\mathbf{r}) e^{j\mathbf{k}_\rho\cdot\boldsymbol{\rho}} dxdy$$
$$F^{-1}[\tilde{f}(\mathbf{k}_\rho; z)] \equiv f(\mathbf{r}) = \frac{1}{(2\pi)^2}\int_{-\infty-\infty}^{+\infty+\infty} \tilde{f}(\mathbf{k}_\rho; z) e^{-j\mathbf{k}_\rho\cdot\boldsymbol{\rho}} dk_x dk_y = S_0(\tilde{f}(\mathbf{k}_\rho)) \tag{4}$$

where

$$S_0(\tilde{f}(\mathbf{k}_\rho)) = \frac{1}{2\pi}\int_0^{+\infty} |\mathbf{k}_\rho| J_0(\mathbf{k}_\rho\cdot\boldsymbol{\rho})\tilde{f}(\mathbf{k}_\rho; z) d|\mathbf{k}_\rho| \tag{5}$$

is referred as a Sommerfeld integral. $J_0$ is the Bessel function of 0 order .

And the Fourier transform between spectrum and spatial domain satisfies Sommerfeld identity and its property, as

$$F\left(\frac{e^{-jk|\mathbf{r}-\mathbf{r}'|}}{4\pi|\mathbf{r}-\mathbf{r}'|}\right) = \frac{e^{-jk_z|z-z'|}}{2jk_z} \tag{6}$$

$$F^{-1}\left\{\begin{matrix}\sin\\ \cos\end{matrix} n\xi\,\tilde{f}(\mathbf{k}_\rho)\right\} = (-j)^n\left\{\begin{matrix}\sin\\ \cos\end{matrix} n\varphi S_n(\tilde{f}(\mathbf{k}_\rho))\right\} \tag{7}$$

where $(\rho, \varphi)$ is the cylindrical coordinates of the projection of the field point on the (x, y) plane. $k_z^2 = k_i^2 - k_\rho^2$, where $k_\rho = \sqrt{k_x^2 + k_y^2}$ and $k_i = \omega\sqrt{\varepsilon_i\mu_i}$. Physically, (4) represented a spherical wave that is expanded as an integral summation of cylindrical waves in the $\rho$ direction, times a plane wave in the z direction.

Apply (4) to (3) and separate the transverse and longitudinal parts of the field, yielding [40]

$$\frac{d\widetilde{\mathbf{E}}_{\boldsymbol{\rho}}}{dz} = \frac{1}{j\omega\varepsilon_0\varepsilon_r}(k_0{}^2\varepsilon_r\mu_r - \mathbf{k}_{\boldsymbol{\rho}}\cdot\mathbf{k}_{\boldsymbol{\rho}}\cdot)(\widetilde{\mathbf{H}}_{\boldsymbol{\rho}}\times\hat{\mathbf{z}}) \mp \frac{J_z}{\omega\varepsilon_0\varepsilon_r}\mathbf{k}_{\boldsymbol{\rho}} - \widetilde{\mathbf{M}}_{\boldsymbol{\rho}}\times\hat{\mathbf{z}} \tag{8}$$

$$\frac{d\widetilde{\mathbf{H}}_{\boldsymbol{\rho}}}{dz} = \frac{1}{j\omega\mu_0\mu_r}(k_0{}^2\varepsilon_r\mu_r - \mathbf{k}_{\boldsymbol{\rho}}\cdot\mathbf{k}_{\boldsymbol{\rho}}\cdot)(\hat{\mathbf{z}}\times\widetilde{\mathbf{E}}_{\boldsymbol{\rho}}) + \frac{\widetilde{M}_z}{\omega\varepsilon_0\varepsilon_r}\mathbf{k}_{\boldsymbol{\rho}} - \hat{\mathbf{z}}\times\widetilde{\mathbf{J}}_{\boldsymbol{\rho}} \tag{9}$$

A rotated coordinate system $(\hat{\mathbf{u}}, \hat{\mathbf{v}})$ is defined based on original spectrum-domain coordinate system $(\mathbf{k}_{\boldsymbol{\rho}}, \hat{z}\times\mathbf{k}_{\boldsymbol{\rho}})$, as [55]

$$\begin{aligned}\hat{\mathbf{u}} &= \frac{k_x}{k_\rho}\hat{\mathbf{x}} + \frac{k_y}{k_\rho}\hat{\mathbf{y}}\\ \hat{\mathbf{v}} &= -\frac{k_y}{k_\rho}\hat{\mathbf{x}} + \frac{k_x}{k_\rho}\hat{\mathbf{y}}\end{aligned} \tag{10}$$

And the transverse electric and magnetic fields can be expressed as

$$\begin{aligned}\widetilde{\mathbf{E}}_\rho &= V^e\hat{\mathbf{u}} + V^h\hat{\mathbf{v}}\\ \widetilde{\mathbf{H}}_\rho\times\hat{z} &= I^e\hat{\mathbf{u}} + I^h\hat{\mathbf{v}}\end{aligned} \tag{11}$$

where $(V^e, I^e)$ and $(V^h, I^h)$ the fields outside the source region are, respectively, TM and TE to z, as shown in Fig. 3.1. By projecting (3.6) and (3.7) on $(\hat{\mathbf{u}}, \hat{\mathbf{v}})$ coordinate, a set of telegraph equation can be obtained, as

$$\begin{aligned}\frac{dV^p}{dz} &= -jk_zZ^pI^p + v^p\\ \frac{dI^p}{dz} &= -jk_zY^pV^p + i^p\end{aligned} \tag{12}$$

where p denotes either e or h type. The characteristic impedance of the transmission line are given as

$$Z^e = \frac{1}{Y^e} = \frac{k_z}{\omega\varepsilon_0\varepsilon_r}$$
$$Z^h = \frac{1}{Y^h} = \frac{\omega\mu_0\mu_r}{k_z} \tag{13}$$

And the voltage and current sources in (12) are given as

$$v^e = \frac{k_\rho}{\omega\varepsilon_0\varepsilon_r}\tilde{J}_z - \tilde{M}_v$$
$$v^h = \tilde{M}_u$$
$$i^e = -\tilde{J}_u$$
$$i^h = -\frac{k_\rho}{\omega\mu_0\mu_r}\tilde{M}_z - \tilde{J}_v \tag{14}$$

The spectral domain electric and magnetic field can be expressed as

$$\tilde{\mathbf{E}} = V^e\hat{\mathbf{u}} + V^h\hat{\mathbf{v}} - \frac{1}{j\omega\varepsilon_0\varepsilon_r}(jk_\rho I^e + \tilde{J}_z)\hat{\mathbf{z}}$$
$$\tilde{\mathbf{H}} = -I^h\hat{\mathbf{u}} + I^e\hat{\mathbf{v}} + \frac{1}{j\omega\mu_0\mu_r}(jk_\rho V^h + \tilde{M}_z)\hat{\mathbf{z}} \tag{15}$$

In the linear media, the fields due to arbitrary current source can be expressed as

$$\tilde{\mathbf{E}} = <\underline{\underline{\tilde{\mathbf{G}}}}_{\mathbf{EJ}}, \tilde{\mathbf{J}}> + <\underline{\underline{\tilde{\mathbf{G}}}}_{\mathbf{EM}}, \tilde{\mathbf{M}}>$$
$$\tilde{\mathbf{H}} = <\underline{\underline{\tilde{\mathbf{G}}}}_{\mathbf{HJ}}, \tilde{\mathbf{J}}> + <\underline{\underline{\tilde{\mathbf{G}}}}_{\mathbf{HM}}, \tilde{\mathbf{M}}> \tag{16}$$

where $\underline{\underline{\tilde{\mathbf{G}}}}_{PQ}$ is the Dyadic Green's function (DGF) relating to P-type field at the source point and Q-type field at the observation point.

Compare (15) and (16) and using (14), the spectrum domain DGF related to fields can be written as

$$\underline{\underline{\widetilde{\mathbf{G}}}}_{\mathbf{EJ}}(\mathbf{k}_{\boldsymbol{\rho}};z\,|\,z') = \begin{bmatrix} -V_i^{\,e} & 0 & \dfrac{k_\rho}{\omega\varepsilon_0\varepsilon_{z'}}V_v^{\,e} \\ 0 & -V_i^{\,h} & 0 \\ \dfrac{k_\rho}{\omega\varepsilon_0\varepsilon_z}I_i^{\,e} & 0 & \dfrac{1}{j\omega\varepsilon_0\varepsilon_{z'}}\left(\dfrac{k_\rho^{\,2}}{j\omega\varepsilon_0\varepsilon_z}I_v^{\,e}-\delta(z-z')\right) \end{bmatrix} \tag{17}$$

$$\underline{\underline{\widetilde{\mathbf{G}}}}_{\mathbf{EM}}(\mathbf{k}_{\boldsymbol{\rho}};z\,|\,z') = \begin{bmatrix} 0 & -V_v^{\,e} & 0 \\ V_v^{\,h} & 0 & -\dfrac{k_\rho}{\omega\mu_0\mu_{z'}}V_i^{\,h} \\ 0 & \dfrac{k_\rho}{\omega\varepsilon_0\varepsilon_z}I_v^{\,e} & 0 \end{bmatrix} \tag{18}$$

$$\underline{\underline{\widetilde{\mathbf{G}}}}_{\mathbf{HJ}}(\mathbf{k}_{\boldsymbol{\rho}};z\,|\,z') = \begin{bmatrix} 0 & I_i^{\,h} & 0 \\ -I_i^{\,e} & 0 & \dfrac{k_\rho}{\omega\varepsilon_0\varepsilon_{z'}}I_v^{\,e} \\ 0 & -\dfrac{k_\rho}{\omega\mu_0\mu_z}V_i^{\,h} & 0 \end{bmatrix} \tag{19}$$

$$\underline{\underline{\widetilde{\mathbf{G}}}}_{\mathbf{HM}}(\mathbf{k}_{\boldsymbol{\rho}};z\,|\,z') = \begin{bmatrix} -I_v^{\,h} & 0 & \dfrac{k_\rho}{\omega\mu_0\mu_{z'}}I_i^{\,h} \\ 0 & -I_v^{\,e} & 0 \\ \dfrac{k_\rho}{\omega\mu_0\mu_z}V_v^{\,h} & 0 & \dfrac{1}{j\omega\mu_0\mu_{z'}}\left(\dfrac{k_\rho^{\,2}}{j\omega\mu_0\mu_z}V_i^{\,h}-\delta(z-z')\right) \end{bmatrix} \tag{20}$$

where $V_i^{\,p}$ and $I_i^{\,p}$ denote voltage and current due to shunt current source while $V_v^{\,p}$ and $I_v^{\,p}$ denote voltage and current due to series voltage source.

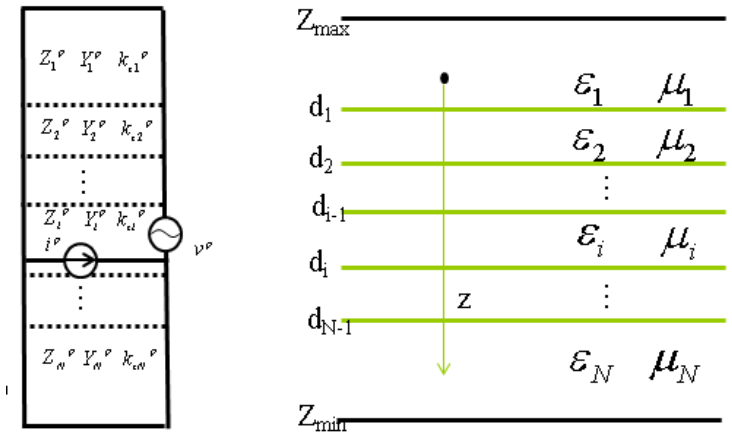


Fig.1 A point source embedded in a general multilayer medium and its transmission line analogy.

Based on the Green's function (17)-(20) for the fields, we will derive the Green's function for vector potential $\mathbf{A}$ and scalar potential $\phi$ with regarding to current and charge, as

$$\begin{aligned}\mathbf{A}(\mathbf{r}) &= \int_{S_i} \underline{\underline{\mathbf{G}}}_{\mathbf{A}}(\mathbf{r},\mathbf{r}')\mathbf{J}(\mathbf{r}')dS' \\ \phi(\mathbf{r}) &= \int_{S_i} G_{\phi}(\mathbf{r},\mathbf{r}')q(\mathbf{r}')dS'\end{aligned} \tag{21}$$

where $\mathbf{r}$ is the observation point while $\mathbf{r}'$ is the source point.

And in the view of current continuity, the Green's function for vector potential $\mathbf{A}$ and scalar potential $\phi$ should always satisfy

$$\frac{1}{\varepsilon_z \mu_z} \nabla \cdot \underline{\underline{\widetilde{\mathbf{G}}}}_{\mathbf{A}} = -\nabla' \widetilde{G}_{\phi} \tag{22}$$

However, in a inhomogeneous medium, the Green's functions for potential $\mathbf{A}$ and $\phi$ satisfying (22) does not in general exist, due to the fact that the scalar potentials of point charges associated with horizontal and vertical current dipoles in a layered medium

are different. Thus, a correction form is introduced to the Green function for vector potentials, as [8]

$$\frac{1}{\varepsilon_z \mu_z} \nabla \cdot \underline{\underline{\mathbf{G}_{\mathbf{A}}}} = -\nabla' G_\phi + P_\phi \hat{z} \tag{23}$$

And define the corrected vector potential Green function as

$$\underline{\underline{\mathbf{K}_{\mathbf{A}}}} = \underline{\underline{\mathbf{G}_{\mathbf{A}}}} + \frac{1}{k^2} \nabla P_\phi \hat{z} \tag{24}$$

Thus, the electric field can be expressed as

$$\mathbf{E} = -j\omega\mu < \underline{\underline{\mathbf{K}_{\mathbf{A}}}}, \mathbf{J} > + \frac{1}{j\omega\varepsilon} \nabla (< G_\phi, \nabla' \cdot \mathbf{J} >) \tag{25}$$

Though the form of $\underline{\underline{\mathbf{G}_{\mathbf{A}}}}$ is not uniquely defined in layer medium problems, the traditional form of $\underline{\underline{\mathbf{G}_{\mathbf{A}}}}$ is chosen as

$$\underline{\underline{\mathbf{G}_{\mathbf{A}}}} = \begin{bmatrix} G_{xx}{}^{A} & 0 & 0 \\ 0 & G_{yy}{}^{A} & 0 \\ G_{zx}{}^{A} & G_{zy}{}^{A} & G_{zz}{}^{A} \end{bmatrix} \tag{26}$$

while the correct $\underline{\underline{\mathbf{K}_{\mathbf{A}}}}$ can be expressed in the form of

$$\underline{\underline{\mathbf{K}_{\mathbf{A}}}} = \begin{bmatrix} G_{xx}{}^{A} & 0 & G_{xz}{}^{A} \\ 0 & G_{yy}{}^{A} & G_{yz}{}^{A} \\ G_{zx}{}^{A} & G_{zy}{}^{A} & G'_{zz}{}^{A} \end{bmatrix} \tag{27}$$

The Green's function for vector potential is associated with the magnetic field by

$$\mu \underline{\underline{\mathbf{G}_{\mathbf{HJ}}}} = \nabla \times \underline{\underline{\mathbf{G}_{\mathbf{A}}}} \tag{28}$$

Using (19) and (28), the spectrum domain $\underline{\underline{\widetilde{\mathbf{G}}_{\mathbf{A}}}}$ can be written as

$$\underline{\underline{\widetilde{\mathbf{G}}}}_{\mathbf{A}} = \begin{bmatrix} \frac{1}{j\omega} V_i^h & 0 & 0 \\ 0 & \frac{1}{j\omega} V_i^h & 0 \\ \frac{\mu_0 \mu_r k_x}{j k_\rho^2} (I_i^h - I_i^e) & \frac{\mu_0 \mu_r k_y}{j k_\rho^2} (I_i^h - I_i^e) & \frac{\mu_0 \mu_r}{j\omega \varepsilon_0 \varepsilon_{r'}} I_v^e \end{bmatrix} \tag{29}$$

$\widetilde{G}_\phi$ and $\widetilde{P}_\phi$ can be obtained from (23) and (29)

$$\widetilde{G}_\phi = \frac{j\omega \varepsilon_0}{k_\rho^2} (V_i^e - V_i^h) \tag{30}$$

$$\widetilde{P}_\phi = \frac{k_0^2 \mu_{z'}}{k_\rho^2} (V_v^e - V_v^h) \tag{31}$$

Finally, $\underline{\underline{\widetilde{\mathbf{K}}}}_{\mathbf{A}}$ from (24) can be written as

$$\underline{\underline{\widetilde{\mathbf{K}}}}_{\mathbf{A}} = \begin{bmatrix} \frac{1}{j\omega} V_i^h & 0 & \frac{j k_x \mu_0 \mu_{r'}}{k_\rho^2} (V_v^e - V_v^h) \\ 0 & \frac{1}{j\omega} V_i^h & \frac{j k_y \mu_0 \mu_{r'}}{k_\rho^2} (V_v^e - V_v^h) \\ \frac{\mu_0 \mu_r k_x}{j k_\rho^2} (I_i^h - I_i^e) & \frac{\mu_0 \mu_r k_y}{j k_\rho^2} (I_i^h - I_i^e) & \frac{\mu_0 \mu_r}{j\omega \varepsilon_0 \varepsilon_{r'}} I_v^e + \frac{-j \mu_0 \mu_{r'}}{k_\rho^2} (-k_z Z_z^e I_v^e + k_z Z_z^h I_v^h) \end{bmatrix} \tag{32}$$

Later, we will show

$$I_i^p(z \mid z') = -V_v^p(z' \mid z) \tag{33}$$

Thus,

$$\underline{\underline{\widetilde{\mathbf{K}}}}_{\mathbf{A}}(r, r') \mu(r') = \underline{\underline{\widetilde{\mathbf{K}}}}_{\mathbf{A}}^{\ t}(r', r) \mu(r) \tag{34}$$

which means $\underline{\underline{\widetilde{\mathbf{K}}}}_{\mathbf{A}}$ satisfies reciprocity.

Now we will derive the solutions of the transmission line voltage and current $V_v^p$, $V_i^p$ and $I_v^p$, $I_i^p$. They satisfy the following equations:

$$\frac{dV_i^p}{dz} = -jk_z Z^p I_i^p \tag{35}$$

$$\frac{dI_i^p}{dz} = -jk_z Y^p V_i^p + \delta(z - z') \tag{36}$$

$$\frac{dV_v^p}{dz} = -jk_z Z^p I_v^p + \delta(z - z') \tag{37}$$

$$\frac{dI_v^p}{dz} = -jk_z Y^p V_v^p \tag{38}$$

where $\delta$ is the Dirac delta function.

Assume the source point at z' is in the m layer and the observation point at z is in the n layer. Layer n is defined with boundaries at $z_{n-1}$ and $z_n$. The propagation constants for m layer and n layer are $k_z^m$, $k_z^n$, respectively. And the characteristic impedance (admittance) are denoted as $Z^m(Y^m)$, $Z^n(Y^n)$, respectively. Assume $z_0 = z_1$ and $z_N = z_{N-1}$. When the source and observation points are in the same layer (m=n), the voltage and current response due to current source can be represented as

$$V_i^p = \frac{Z_n^p}{2}[e^{-jk_z^n|z-z'|} + M_n^p \sum_{s=1}^{4} B_{ns}^p e^{-jk_z^n \gamma_{ns}}] \tag{39}$$

$$I_i^p = \frac{1}{2}[\pm e^{-jk_z^n|z-z'|} + M_n^p \sum_{s=1}^{4} (-1)^s B_{ns}^p e^{-jk_z^n \gamma_{ns}}] \tag{40}$$

where the upper and lower signs pertain to z>z'and z<z', respectively. And

$$M_n^{\ p} = \frac{1}{[1-\widetilde{R}^{p}{}_{n,n-1}\widetilde{R}^{p}{}_{n,n+1}e^{-2jk_z^{\ n}(z_n-z_{n-1})}]}$$

$$B_{n1}^{\ p} = \widetilde{R}^{p}{}_{n,n+1}, \qquad \gamma_{n1}^{\ p} = 2z_n - (z+z')$$

$$B_{n2}^{\ p} = \widetilde{R}^{p}{}_{n,n-1}, \qquad \gamma_{n2}^{\ p} = -2z_{n-1} + (z+z')$$

$$B_{n3}^{\ p} = \widetilde{R}^{p}{}_{n,n-1}\widetilde{R}^{p}{}_{n,n+1}, \qquad \gamma_{n3}^{\ p} = 2(z_n - z_{n-1}) - (z-z')$$

$$B_{n4}^{\ p} = \widetilde{R}^{p}{}_{n,n-1}\widetilde{R}^{p}{}_{n,n+1}, \qquad \gamma_{n4}^{\ p} = 2(z_n - z_{n-1}) + (z-z')$$

And the generalized reflection coefficients are given as

$$\widetilde{R}^{p}{}_{n,n-1} = \frac{R^{p}{}_{n,n-1} + \widetilde{R}^{p}{}_{n-1,n-2}e^{-2jk_z^{\ n-1}(z_{n-1}-z_{n-2})}}{1 + R^{p}{}_{n,n-1}\widetilde{R}^{p}{}_{n-1,n-2}e^{-2jk_z^{\ n-1}(z_{n-1}-z_{n-2})}} \tag{41}$$

$$\widetilde{R}^{p}{}_{n,n+1} = \frac{R^{p}{}_{n,n+1} + \widetilde{R}^{p}{}_{n+1,n+2}e^{-2jk_z^{\ n+1}(z_{n+1}-z_n)}}{1 + R^{p}{}_{n,n+1}\widetilde{R}^{p}{}_{n+1,n+2}e^{-2jk_z^{\ n+1}(z_{n+1}-z_n)}} \tag{42}$$

where

$$R^{p}{}_{n,n-1} = \frac{Z^{p}{}_{n-1} - Z^{p}{}_{n}}{Z^{p}{}_{n-1} + Z^{p}{}_{n}} \tag{43}$$

$$R^{p}{}_{n,n+1} = \frac{Z^{p}{}_{n+1} - Z^{p}{}_{n}}{Z^{p}{}_{n+1} + Z^{p}{}_{n}} \tag{44}$$

Consider the next case m<n, and the source point is above the observation point (z'<z), the final solutions of $V_i^{\ p}$ and $I_i^{\ p}$ are

$$V_i^{\ p} = \{\frac{Z_m^{\ p}}{2} T_{mn}^{\ p,down}[e^{-jk_z^{\ m}(z_m-z')} + \widetilde{R}^{p}{}_{m,m-1}e^{-jk_z^{\ m}(-2z_{m-1}+z_m+z')}]\cdot$$
$$[e^{-jk_z^{\ n}(-z_{n-1}+z)} + \widetilde{R}^{p}{}_{n,n+1}e^{-jk_z^{\ n}(-z_{n-1}+2z_n-z)}]\cdot M_m^{\ p}\} \tag{45}$$

$$I_i^p = \{\frac{Z_m^p}{2} T_{mn}^{p,down} Y_n^p [e^{-jk_z^m(z_m - z')} + \widetilde{R}^p{}_{m,m-1} e^{-jk_z^m(-2z_{m-1}+z_m+z')}] \cdot$$
$$[e^{-jk_z^n(-z_{n-1}+z)} - \widetilde{R}^p{}_{n,n+1} e^{-jk_z^n(-z_{n-1}+2z_n-z)}] \cdot M_m^p\} \tag{46}$$

where $T_{mn}^{p,down}$ is the generalized transmission coefficient from layer m to layer n, with

$$T_{mn}^{p,down} = \prod_{i=m}^{n-1} e^{-jk_z^i(z_i - z_{i-1})} S_{i,i+1}^{p,down} \tag{47}$$

where we assume $z_{m-1} = z_m$ and

$$S_{i,i+1}^{p,down} = \frac{R^p{}_{i,i+1} + 1}{1 - R^p{}_{i+1,i} \widetilde{R}^p{}_{i+1,i+2} e^{-2jk_z^{i+1}(z_{i+1} - z_i)}} \tag{48}$$

Similarly, when m>n, and the source point is below the observation point (z'>z), the final solutions of $V_i^p$ and $I_i^p$ are

$$V_i^p = \{\frac{Z_m^p}{2} T_{mn}^{p,up} [e^{-jk_z^m(-z_{m-1}+z')} + \widetilde{R}^p{}_{m,m+1} e^{-jk_z^m(2z_m - z_{m-1} - z')}] \cdot$$
$$[e^{-jk_z^n(z_n - z)} + \widetilde{R}^p{}_{n,n-1} e^{-jk_z^n(-2z_{n-1}+z_n+z)}] \cdot M_m^p\} \tag{49}$$

$$I_i^p = \{\frac{Z_m^p}{2} T_{mn}^{p,up} Y_n^p [e^{-jk_z^m(-z_{m-1}+z')} + \widetilde{R}^p{}_{m,m+1} e^{-jk_z^m(2z_m - z_{m-1} - z')}] \cdot$$
$$[-e^{-jk_z^n(z_n - z)} + \widetilde{R}^p{}_{n,n-1} e^{-jk_z^n(-2z_{n-1}+z_n+z)}] \cdot M_m^p\} \tag{50}$$

where $T_{mn}^{p,up}$ is

$$T_{mn}^{p,up} = \prod_{i=n+1}^{m} e^{-jk_z^i(z_i - z_{i-1})} S_{i,i-1}^{p,up} \tag{51}$$

We assume $z_{m-1} = z_m$ and

$$S_{i,i-1}^{p,up} = \frac{R^{p}_{i,i-1} + 1}{1 - R^{p}_{i-1,i}\tilde{R}^{p}_{i-1,i-2}e^{-2jk_z^{i-1}(z_{i-1}-z_{i-2})}} \tag{52}$$

$V_v^p$ and $I_v^p$ can be calculated from $V_i^p$ and $I_i^p$ by duality, with the following substitution:

$$V_i^p -> I_v^p, I_i^p -> V_v^p, Z^p -> Y^p, Y^p -> Z^p \tag{53}$$

(33) could be demonstrated with (50) and reciprocity of (34)- (37).

The spectral-domain Green function through the procedure above is validated using a two-layered media with GND bottom. The geometry is shown in Fig. 2. The frequency is 60 GHz. Fig 3 shows the results comparison between the Green function from the general methods developed above and analytical form in [23]. Good correlation has been achieved for spectrum-domain Green function for magnetic potential in x-x direction.

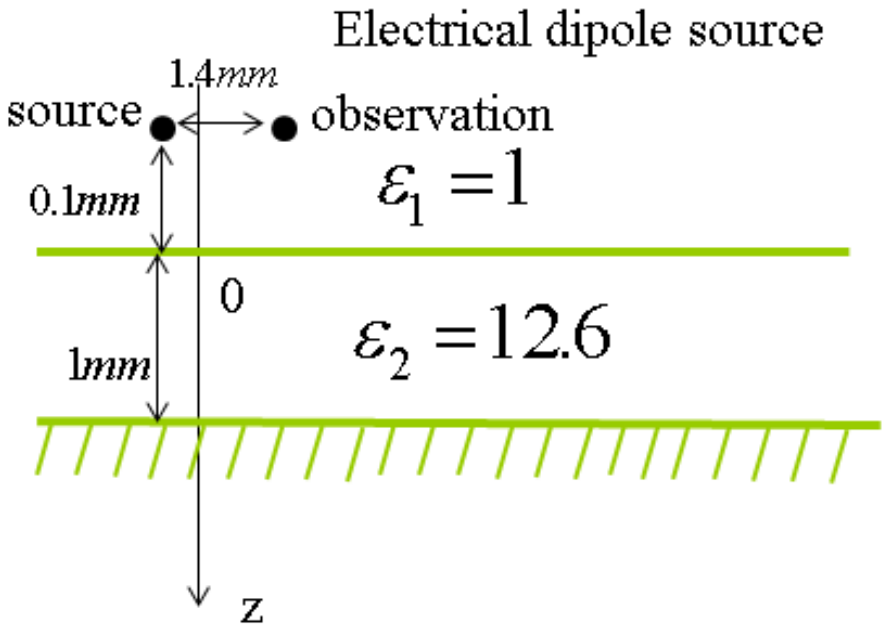


Fig. 2 Example of two-layered media with ground bottom.

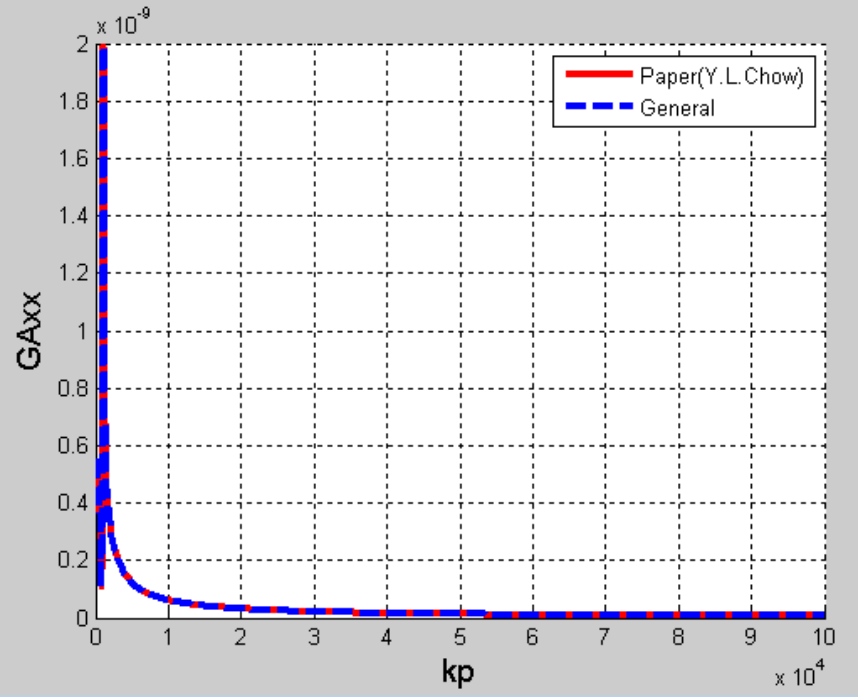


Fig. 3. Comparison of spectrum-domain $\tilde{G}_{xx}^{A}$ using the approach discussed in this paper and analytical form from Y. Chow's paper [27].

## III. DISCRETE COMPLEX IMAGE METHOD FOR SOMMERFELDINTEGRATION

Due to the nature of the kernel of the Sommerfeld integration, direct numerical integration is almost impossible for wide-band analysis. Meanwhile, the singular points at the real axis of kp plane further impede the direct calculations of Sommerfeld integration. Discrete complex image method was developed for decades to analytically calculate Sommerfeld integration by utilizing Sommerfeld identity. As shown in [4], [5], [23]~[27], the spatial-domain Green function of general layered media could be written as

$$G = G_{pri} + G_{static} + G_{sw} + G_{sp} \tag{54}$$

where $G_{pri}$ is the primary filed from observation and source points, which is same as the free-space Green's function with retarded terms. $G_{static}$ is the quasi-static portion that assumes $k_\rho \to \infty$. $G_{sw}$ represents the term of surface wave, which is the poles in the $k_\rho$ and dominates mainly in the far field region. $G_{sp}$ is calculated based on the Sommerfeld identity with complex images and physically represents spherical waves in the space. The following paragraph will analyze each term in details.

The first term in (3.49) only exists the two conditions satisfy, 1) the source and observation points are in the same layer. 2) there is filed coupling between source and observation if assuming free space. However, even for the cases source and observation points are in the different layers, the term of primary filed is still needed. The primary field can be obtained with the aid of the Sommerfeld identity, as

$$G_{pri} = \frac{e^{-jk_m r}}{4\pi r} = \frac{1}{2\pi}\int_0^\infty \widetilde{G}_{pri} J_0(k_\rho \rho) k_\rho dk_\rho = \frac{1}{2\pi}\int_0^\infty \frac{e^{-jk_z{}^m|z|}}{2jk_z{}^m} J_0(k_\rho \rho) k_\rho dk_\rho \tag{55}$$

where the source point is located in m layer and r is the distance between source and observation points.

For the quasi-static $G_{static}$, the analytical form is only available for simple geometries if we assume frequency is approaching 0. Generally, the spectrum-domain Green function be expanded, through M order GPOF algorithm, as [27]

$$\widetilde{G}(k_p) = \frac{A_0 + A_1 e^{-a_1 k_z{}^m} + A_2 e^{-a_2 k_z{}^m} + \ldots + A_M e^{-a_M k_z{}^m}}{2jk_z{}^1} \tag{56}$$

When $k_\rho \to \infty$,

$$\widetilde{G}_{static} = \frac{A_0}{2jk_z^{\ 1}} \tag{57}$$

which corresponds to the quasi-static counterpart in the spectrum domain. And apply $\widetilde{G}_{static}$ for the kernel of the Sommerfeld integration, we can obtain

$$G_{static} = A_0 \frac{e^{-jk_1\rho}}{4\pi\rho} \tag{58}$$

where $\rho$ is the distance between the source and observation points in the x-y plane.

The spectrum-domain $\widetilde{G}(k_p)$ has poles which make it difficult to be integrated along a certain path. The poles along the integration path are associated with surface wave, which are actually the residues for the poles. Moreover, for the geometry shown in Fig. 3.1 ($Z_{\max} \to \infty$ and $Z_{\min}$ is finite), there are two kinds of modes. The guided modes is constrained by the layered slab, with energy bound to the slab. They are evanescent modes in region 1 with $k_{z1} < k_1$. Those guided modes behave in the manner of cylindrical waves and correspond to surface wave. And the other unguided modes can propagate in region 1 with $k_{z1} > k_1$. They behave as spherical waves and can be approximated using complex images. Without surface wave extraction, it is physically inappropriate to approximate cylindrical surface waves using spherical waves in the far field region [20].

Considering the Sommerfeld integration paths for multi-layer media in Fig. 3.4, there is a branch cut associated with k1. The selection of branch cut could be flexible, but in order to clearly explain the modes with surface wave and spherical wave, we choose the branch cut mostly lies on the y axis, as shown in Fig. 3.4. It could be noted for any of the poles, the real part of $k_{\rho\rho}$ is larger than $k_1$, which indicates the z-dependence of each

residue is an exponentially decaying function. Thus, surface waves which related to those residues are evanescent modes. On the other hand, all the $k_\rho$ along the integration path c1 in Fig. 3.4 have a real part smaller than $k_1$, which is corresponding to spatial wave propagating at z direction. The surface wave modes and spatial wave modes are orthogonal, as stated in [23].

For multilayer media, only the unbounded layer has branch cut, as in the bounded layer, wave could travel to both directions. $k_z^m$ is not a double-value function if m is a bounded layer. For the unbounded region 1 in Fig. 3.1, the Riemann sheet needs to be determined for the branch cut. In order to satisfy the radiation condition, we need to ensure

$$\mathrm{Im}(k_z^1) < 0 \tag{59}$$

The procedure to implement surface wave pole extraction is shown below:

The locations of surface wave poles are detected numerically. Along the real axis of kp, firstly local maximum points are picked out numerically.

Next, contour integration is used to judge whether those maximum points are poles. Calculate and save the residue for real poles.

After determine the real pole location, a further refine of the step is needed to the local pole region to improve the precisions of finding more accurate poles.

Calculate $\widetilde{G}_{sw}$ for surface wave part in the spectrum domain. Due to the conjugation of the surface wave poles, $\widetilde{G}_{sw}$ can be expressed as

$$\widetilde{G}_{sw} = \sum_p \frac{2k_p \,\mathrm{Re}\, s_p}{k_p^2 - k_{pp}^2} \tag{60}$$

The spatial-domain surface wave term could be calculated as

$$G_{sw} = \sum_{p} \frac{-2\pi j \mathrm{Res}_{\mathrm{p}}}{4\pi} H^{(2)}{}_{0}(k_{\rho\rho_p}\rho) k_{\rho\rho_p} \tag{61}$$

where $k_{\rho\rho_p}$ is the p th pole refined from step (4).

The 1-D methods above only search the poles along real axis of $k_\rho$, which would be only suitable for lossless medium. When dealing with lossy medium, methods with recursive contour integration in the entire $k_\rho$ plane were first proposed in [31] to extract poles. Recently, a general method with a new criteria for pole extractions is developed in [61].

However, if we expand the spatial wave (branch cut) with surface wave extraction, the Green function in near-filed region will show inaccuracy, as the singularity in the surface-wave term is weaker than that in the primary field. In the far field, as the surface-wave propagation at a rate of $\sqrt{\rho}$ while the spatial wave decays exponentially, the affects of surface wave dominant. A transition point is proposed in [31] to determine the criteria whether the surface-wave terms should be extracted. Teo discussed error analysis for the DCIM with and without surface-wave pole extractions and proposed a new form that is suitable for both near and far fields [27].

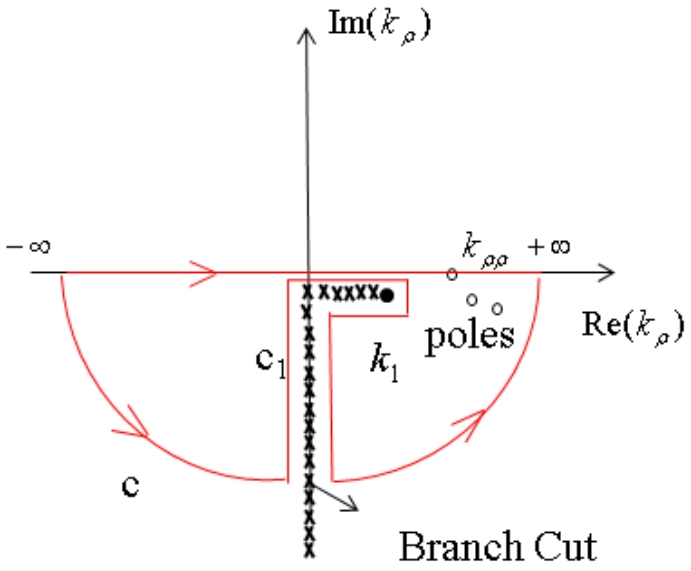


Fig. 4 Integration path for Sommerfeld kernel in $k_\rho$ plane

For the example shown in Fig. 4, the spectrum-domain Green Function in xx direction along real axis of kp is plotted in Fig. 5 (a), from where there is a pole when $k_p = 1100$. Fig. 5 (b) shows the kernel of SI integration with the same Green Function after subtraction of the surface-wave pole.

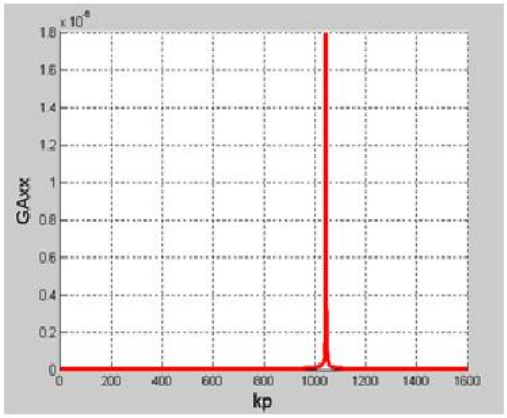


(a)

Fig. 5 Surface-wave pole of the spectrum-domain Green Function for layered structure shown in Fig. 2. (a) Green Function without pole extraction

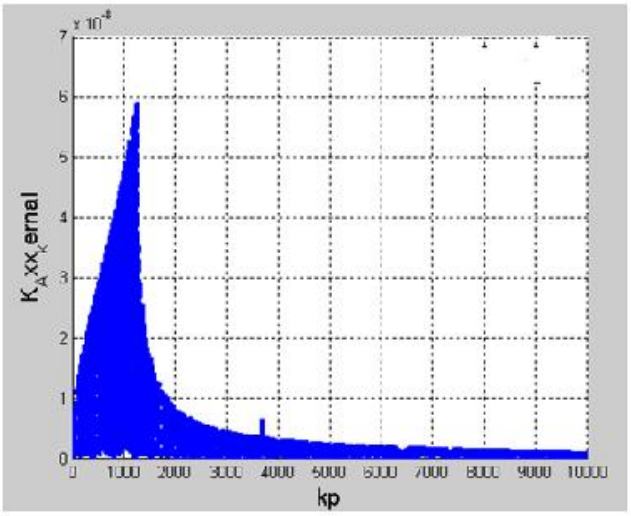


(b)

Fig. 5 Surface-wave pole of the spectrum-domain Green Function for layered structure shown in Fig. 2. (a) Green Function without pole extraction (b) Kernel of SI with pole extraction. (cont.)

After subtraction of primary field, quasi-static term and surface-wave poles, the remaining portion of the spectrum-domain Green Function could be written in the form of spherical waves with complex distance of its images, as

$$\widetilde{G}_{sp} = \sum_{i=1}^{N_G} a_i e^{-b_i k^1{}_z} \tag{62}$$

where the integration path is formed by uniform samples along [23]

$$k_z^{\,1} = k_1[-jt + (1 - t/T_0)] \tag{63}$$

where t is a running parameter from 0 to $T_0$ to represent a complex variable $k_z^{\,1}$. The complex function $\widetilde{G}_{comp}$ with real variable t could be approximated by the summation of exponential functions, using GPOF [27]. Thus, the spatial-domain Green Function that is related to spherical waves can be easily obtained through Sommerfeld identity, as

$$G_{sp} = \frac{1}{4\pi}\sum_{i=1}^{N_G} a_i \frac{e^{-jk_1 r_i}}{r_i} \tag{64}$$

where

$$r_i = \sqrt{\rho^2 + (-jb_i)^2} \tag{65}$$

The accuracy of the GPOF is related to the value of $T_0$ and number of sampling points. Aksun proposed a two-level approach with modified Sommerfeld integration path for robust GPOF applied to layered media [26].

For the unbounded layered media as shown in Fig. 3.2, the spherical wave expansion should be only regarding to radiated waves in the unbounded media [27]. In the bounded layer, wave could travel to both directions and no branch cut will be associated with wave numbers. Thus, expansion of spherical wave regarding to the wave number will introduce new branch cut, which can be corrected to expand the spherical waves only in the unbounded region, i.e. $k_z^1$ for all the analysis in this paper.

In summary, by applying discrete complex image method, the spectrum-domain Green function has general form as

$$\widetilde{G} = \widetilde{G}_{pri} + \widetilde{G}_{static} + \widetilde{G}_{sw} + \widetilde{G}_{sp} \tag{66}$$

where its spatial counterpart is shown as equation (3.49).

The geometry shown in Fig. 4 is used as the first example to validate the formulation and procedure discussed above in Charters 2 and 3. The frequency is 60 GHz. Fig. 6 compares the final results of spatial-domain Green Functions from the formulation in this paper and the analytical forms in Ref [50]. Good correlations have

been achieved. Fig. 7 shows the contributions of each term in equation (3.49) relative to the distance between source and observation points.

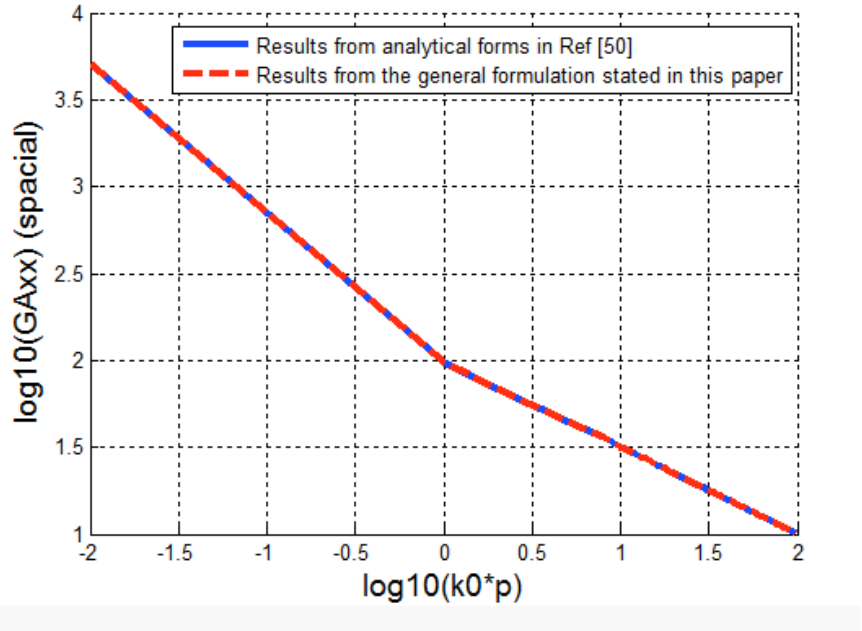


Fig. 6 Correlations of the spatial-domain Green Function for layered media structure shown in Fig. 2.

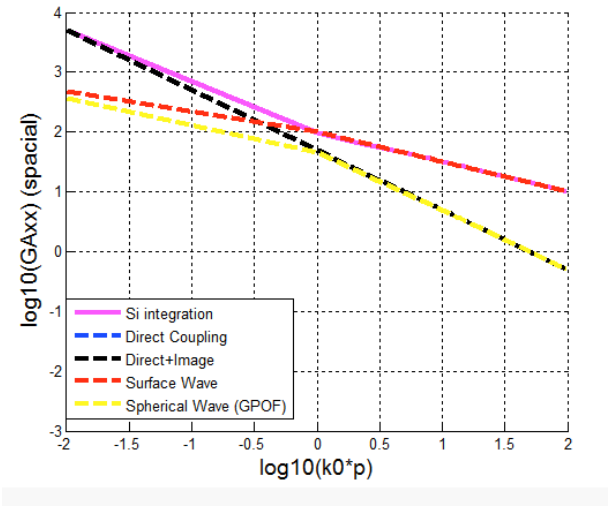


Fig. 7 Contributions of primary field, quasi-static term, surface-wave poles and complex images to the spatial-domain Green Function.

A four-layer media shown in Fig. 8 and Fig. 10 is used as the second example, same as the examples used in [25]. All the geometry details and material properties are shown in the figures. For the example in Fig. 8, the source and observation points are in different layer while source and observation overlaps in Fig. 10. Fig. 9 and Fig. 10 shows the spatial-domain Green Function for magnetic potential A in xx direction. The results in blue is from the calculations of DCIM without surface wave poles while the results in red is calculated from DCIM with surface poles.

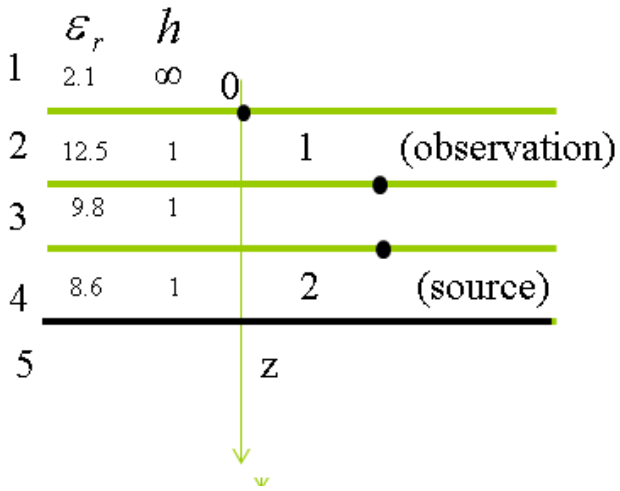


Fig. 8 A four-layer media with source and observation points in the different layer

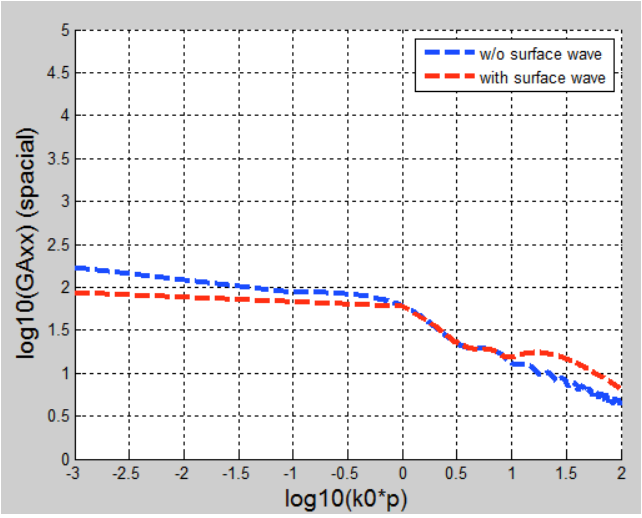


Fig. 9 Spatial-domain Green Function $G_{Axx}$ for layered media structure shown in Fig. 8.

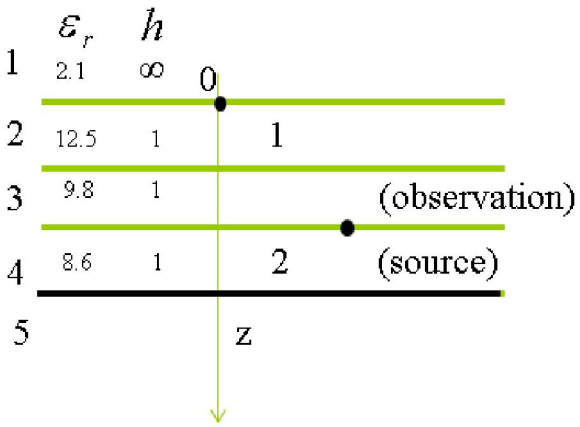


Fig. 10 A four-layer media with source and observation points at the same location

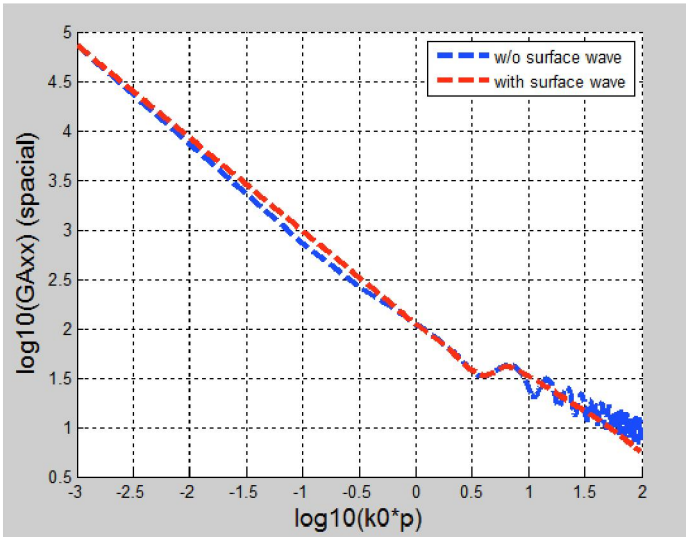


Fig. 11 Spatial-domain Green Function $G_{Axx}$ for layered media structure shown in Fig. 10.

A five-layer media shown in Fig. 12 is used to calculate electrical potential Green function $G_\phi$ as the third example, same as the examples used in [31]. The source point is at z=1.4 while the observation point is at z'=0.4. The frequency is 30 GHz. Fig.13 shows the spatial-domain Green Function $G_\phi$ with and without surface wave extracted.

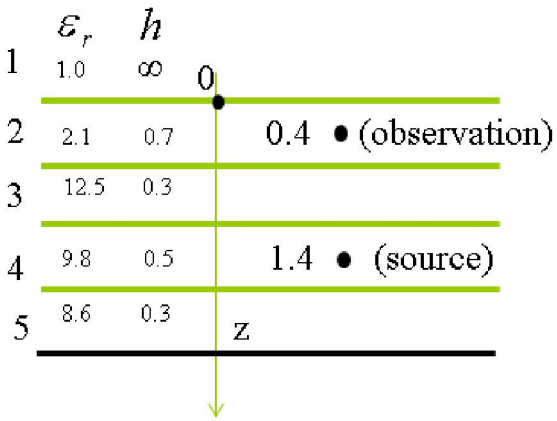


Fig. 12 A five-layer media with source and observation points in the different layer

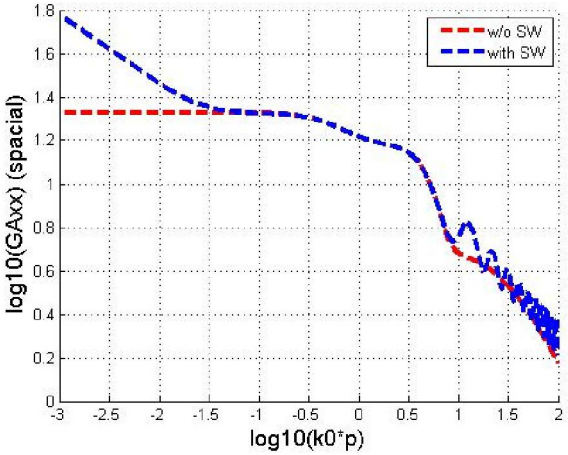


Fig. 13 Spatial-domain Green Function $G_\phi$ for layered media structure shown in Fig. 12.

## IV. Modelling guideline for applications of 3D IC

Fig.14 showed an example of the geometry of 3DIC. It is 4-layer DRAM with one layer of interposer at the bottom of the IC chip. The chip is integrated with a 2.5 D silicon interposer through TSVs. The interposer is soldered on a PCB using BGA. There is a ground layer at the bottom of the PCB. All the DRAM, logic and interposer layers are silicon layers. The permeability of the silicon is 11.9. The conductivity of DRAM and

logic layers are 1 S/m. The conductivity of Silicon interposer is 0.1 S/m. The PCB layer contains FR4, which has permeability of 4.4. The thickness of every DRAM layer is 270 um. The thickness of logic layer, interposer and PCB is 50 um, 200 um, and 2mm respectively. The source point is at DRAM layer and the observation layer is at interposer. The top layer is air.

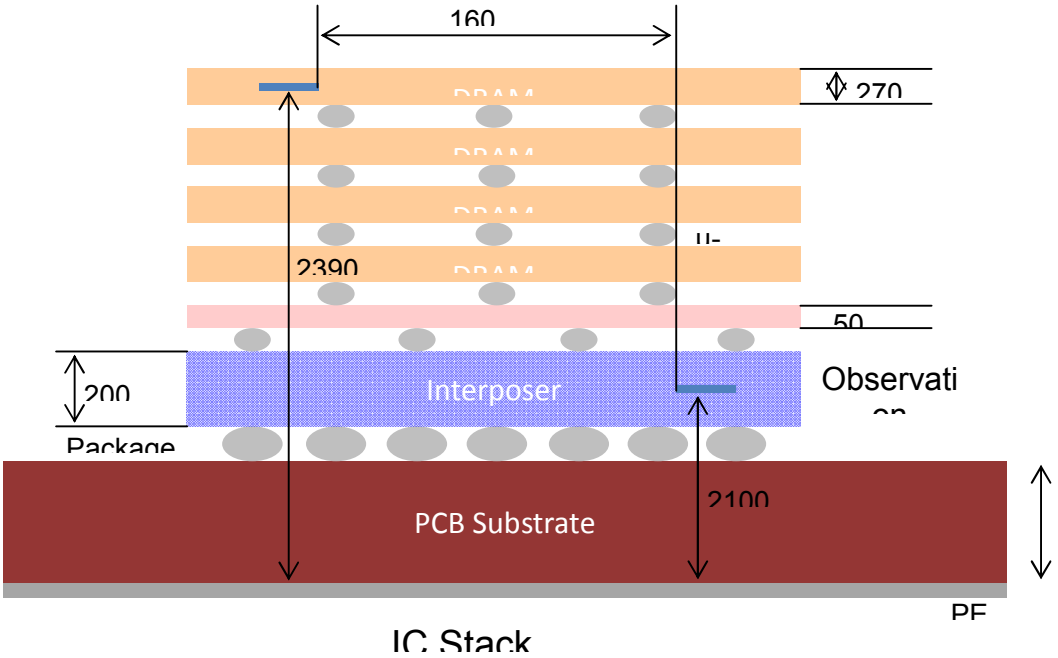


Fig. 14 The geometry of 3D memory IC integrated on 2.5D silicon interposer

Fig. 15 and Fig. 16 are the plots of the spacial Green function for vector magnetic potential and electric potential at the frequency of 30kHz, 30MHz and 30 GHz. When the source and observation points are very closed to each other, the primary term dominates the Green function, which means the effects of multi-layer media cannot be shown for points with small distance. At relative low frequency, one quasi-static image caused by PCB ground plane generates dominant effects to the Green functions of magnetic potentials, when the observation point is further from source point. However, when frequency increase, image due to lossy media has complex distance, so in Fig 15, the total

layered Green function divert with purely image effect at 30MHz when the distance is large. For electric potential, since layers with different permeability generates multiple images, the overall effects need to be considered within spherical wave effect even when the frequency is low, although it is still quasi-static field. At the frequency of 30G, surface wave becomes to show up at far field but the magnitude is very low and can be generally ignored by this application. When the distance of the source and observation point is far, the coupling effects is much larger as spherical wave begins to dominate.

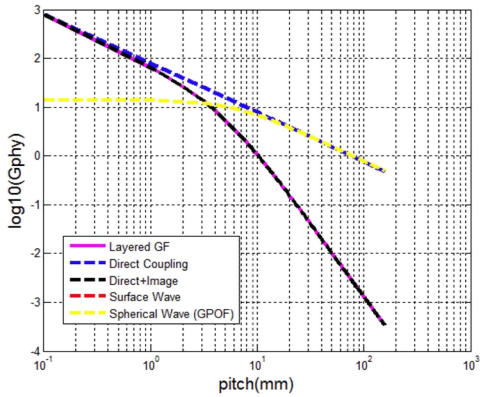


(a)

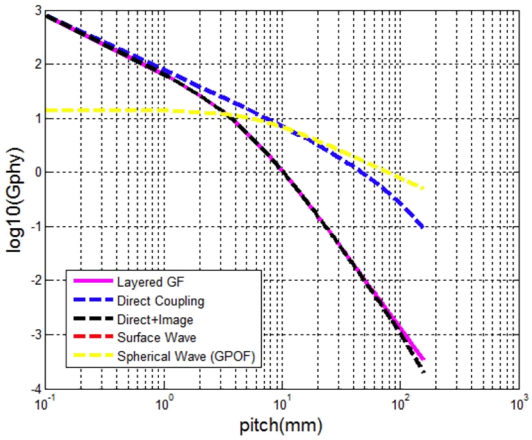


(b)

Fig. 15 the spacial Green function for vector magnetic potential at the frequency of (a) 30kHz, (b) 30MHz and (c) 30 GHz

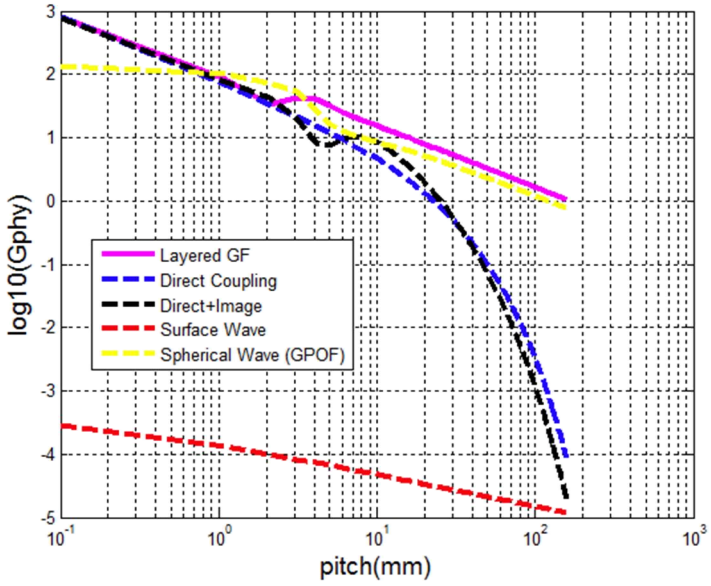


(c)

Fig. 15 the spacial Green function for vector magnetic potential at the frequency of (a) 30kHz, (b) 30MHz and (c) 30 GHz(cont.)

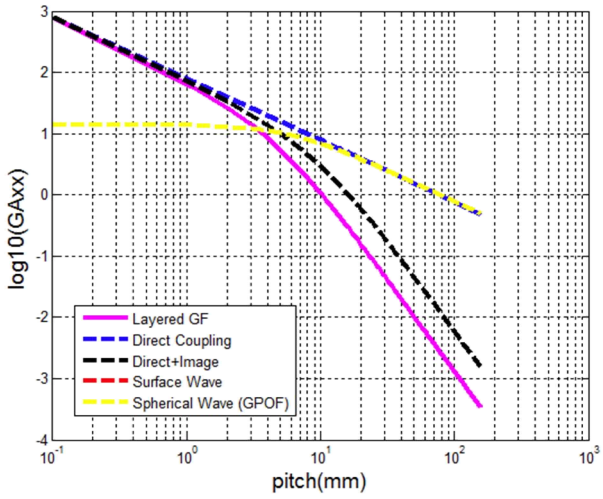


(a)

Fig. 16 the spacial Green function for electric potential at the frequency of (a) 30kHz, (b) 30MHz and (c) 30 GHz

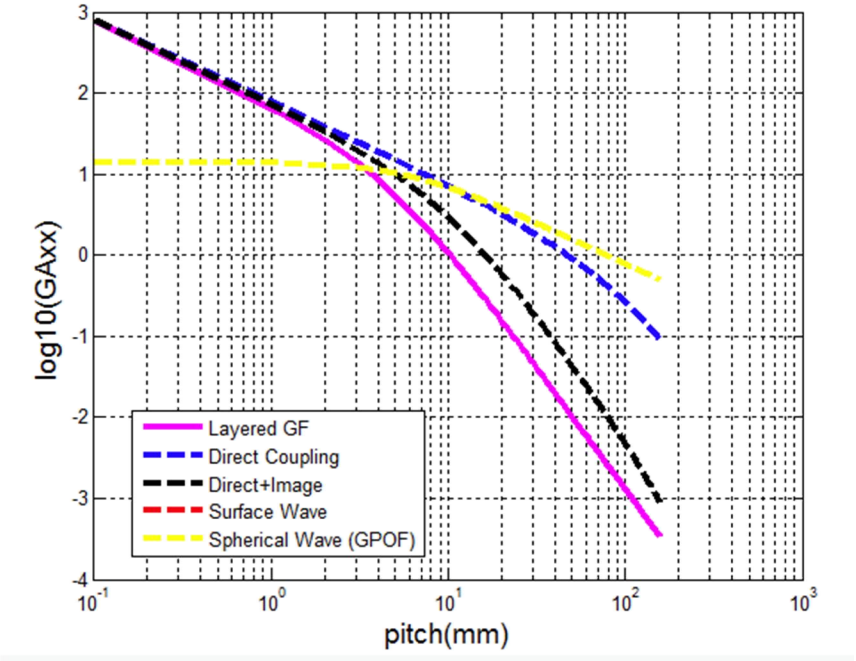


(b)

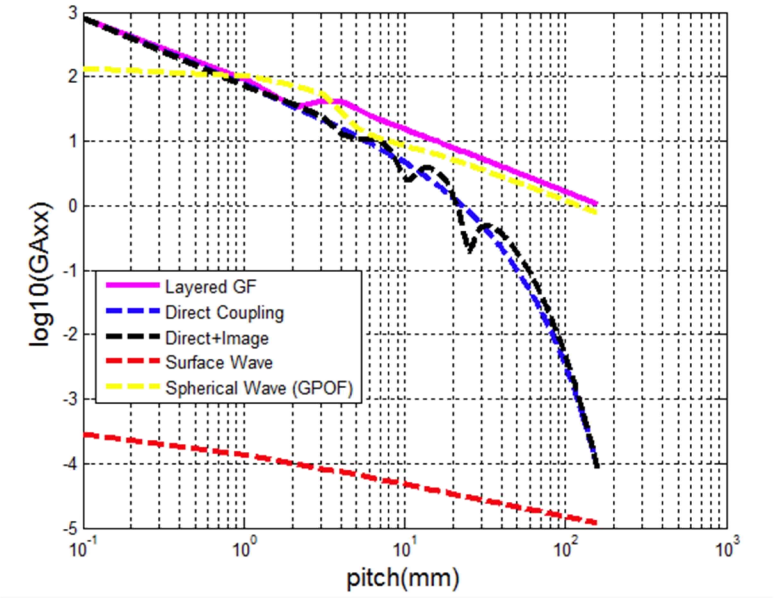


(c)

Fig. 16 the spacial Green function for electric potential at the frequency of (a) 30kHz, (b) 30MHz and (c) 30 GHz(cont.)

## V. CONCLUSION

In this paper, we reviewed previous method of deriving Green function in multi-layer media. DCIM has been used to derive the Green function with lossy media. The study of applying the methods to the real applications of 3DIC shows at image theories can be applied to magnetic vector Green functions at low frequency, however, multiple images should be considered for electric potential Green's function. At high frequency, surface-wave term has far-field effects when the distance of the interconnect is far. Spatial-wave term becomes to dominate when the pitch size becomes larger.

## REFERENCES

[1] K. Banerjee, S. Souri, P. Kapur, and K. Saraswat, "3-D IC: a novel chip design for improving deep-submicrometer interconnect performance and systems-on-chip integration," Proceedings of the IEEE, vol. 89, no. 5, pp. 602-633, 2001.

[2] K. Bernstein, P. Andry, J. Cann, P. Emma, D. Greenberg, W. Haensch, M. Ignatowski, S. Koester, J. Magerlein, R. PURI, and A. Young, "Interconnects in the third dimension: Design challenges for 3D ICs," Design Automation Conference, 2007.

[3] C. A. Balanis, "Advanced engineering electromagnetics," New York: John Wiley & Sons, 1989.

[4] L. Feng, and J. Jin "Discrete complex image method for green's functions of general multilayer media," IEEE Microwave and Guided Wave Letters, Vol. 10, No 10, Oct. 2000.

[5] V. Okhmatovski, A. Cangellaris, "A new technique for the derivation of closed-form electromagnetic green's function for unbounded planar layered media," IEEE Trans. Antennas and Propagation, vol. 50, no. 7, July. 2002.

[6] J. R. Mosig, "Arbitrarily shaped microstrip structures and their analysis with a mixed potential integral equation," IEEE Trans. Microwave Theory Tech., vol. 36, pp. 314-323, Feb. 1988

[7] D. C. Chang and J. X. Zhang, "Electromagnetic modeling of passive circuit elements in MMIC," IEEE Trans. Microwave Theory Tech., vol. 40, pp. 1741-1747, Sep. 1992.

[8] K. A. Michalski and D. Zheng, "Electromagnetic scattering and radiation by surfaces of arbitrary shape in layered media," IEEE Trans. Antennas and Propagation, vol. 38, pp. 335-352, Mar. 1990.

[9] A. Weisshaar, H. Lan, A. Luoh, "Accurate Closed-Form Expressions for the Frequency-Dependent Line Parameters of On-Chip Interconnects on Lossy Silicon Substrate," IEEE Trans. Advanced Packing., vol. 25, no 2, May. 2002.

[10] C. Xu, H. Li, R. Suaya and K. Banerjee, "Compact AC modeling and performance analysis of through-silicon vias in 3-D ICs," IEEE Trans. Electron Devices, vol. 57, no. 12, Dec. 2010.

[11] A. F. Benner, P. K. Pepeljugoski, and R. J. Recio, "A roadmap to 100G Ethernet at the enterprise datacenter, " IEEE Commun. Mag. vol. 45, no.11, pp. 10-17, Nov. 2007.

[12] W. C. Chew, "Wave and Fields in Inhomogeneous Media," IEEE Press, NJ, 1995.

[13] K. Michalski, and J. Mosig, "Multilayered media green's functions in integral equation formulations," IEEE Trans. Antennas and Propagation, vol. 45, no.3, Mar. 1997.

[14] W. C. Chew and Q. Liu, “Resonance frequency of a rectangular microstrip patch,” IEEE Trans. Antennas Propagat., vol. 36, pp. 1045–1056, Aug. 1988.

[15] T.-S. Horng, N. G. Alexopoulos, S.-C. Wu, and H.-Y. Yang, “Fullwave spectral analysis for open microstrip discontinuities of arbitrary shape including radiation and surface-wave losses,” Int. J. Microwave Millimeter-Wave Comput.-Aided Eng., vol. 2, no. 4, pp. 224–240, 1992.

[16] T. Becks and I. Wolff, “Analysis of 3-D metallization structures by a full-wave spectral domain technique,” IEEE Trans. Microwave Theory Tech., vol. 40, pp. 2219–2227, Dec. 1992.

[17] K. A. Michalski and D. Zheng, “Analysis of planar microstrip structures of arbitrary shape—To be, or not to be in the spectral domain?,” in Proc. Symp. Antennas Tech. Applicat. Electromagn., Winnipeg, Canada, Aug. 1990.

[18] B. Hu and W. C. Chew, “Fast inhomogeneous plane wave algorithm for electromagnetic solutions in layered medium structures—2D case,” Radio Sci., vol. 35, no. 1, 2000.

[19] T. J. Cui and W. C. Chew, “Fast evaluation of Sommerfeld integrals for EM scattering and radiation by three-dimensional buried objects,” IEEE Geosci. Remote Sensing, vol. 37, pp. 887–900, Mar. 1999.

[20] A. C. Cangellaris and V. I. Okhmatovski, “New closed-form Green’s function in shielded planar layered media,” IEEE Trans. Microwave Theory Tech., vol. 48, pp. 2225–2232, Dec. 2000.

[21] Q.-H. Liu and W. C. Chew, “Application of the conjugate gradient fast Fourier transfer method with an improved fast Hankel transform algorithm,” Radio Sci., vol. 29, pp. 1009–1022, July–Aug. 1994.

[22] W. Cai and T. Yu, “Fast calculation of Dyadic Green function for electromagnetic scattering in a multilayered medium”, J. Comput. Phy., Nov. 1991.

[23] Y. Chow, J. Yang, D. Fang, G. E. Howard, “A closed-form Spatial Green’s Function for the Thick Microstrip Substrate”, IEEE Trans. Microwave Theory and Techniques, vol. 39, no 3, Mar. 1991.

[24] M. Irsadi, Aksun, and R. Mittra “Derivation of closed-form Green’s function for a general microstrip geometry”, IEEE Trans. Microwave Theory and Techniques, vol. 40, no 11, Nov. 1992.

[25] G. Dural, and M. Aksun, “Closed-Form Green’s Function for General Sources and Stratified Media”, IEEE Trans. Microwave Theory and Techniques, vol. 43, no 7, Jul. 1995.

[26] M. Aksun, “A Robust Approach for the Derivation of Closed-Form Green’s Function”, IEEE Trans. Microwave Theory and Techniques, vol. 44, no 5, May 1996.

[27] M. Yuan, T. Sarkar, M. Salazar-Palma, “A direct discrete complex image method from the closed-form Green’s functions in multilayered media”, IEEE Trans. Microwave Theory and Techniques, vol. 54, no 3, Mar. 2006.

[28] T. Itoh, “Spectral-domain immittance approach for dispersion characteristics of generalized printed transmission lines”, IEEE Trans. Microwave Theory and Techniques, vol. MTT-28, July 1980.

# II. AN EFFICIENT METHOD TO EXTRACT SURFACE-WAVE POLES OF GREEN'S FUNCTIONS NEAR BRANCH CUT IN LOSSY LAYERED MEDIA

Siming Pan, and Jun Fan

***Abstract*—**Calculating the Green's functions in lossy layered media using the discrete complex image method (DCIM) is challenging, due to the difficulties in extracting the surface-wave poles that are very close to a branch cut. An efficient algorithm based on the contour method is proposed in this paper to locate these poles and calculate the residues. The proposed method is robust for both the lossless and lossy media. With the proposed approach, it is shown in numerical examples that some poles, very close to a branch cut, are successfully extracted that were missed using the previous techniques proposed in [7] in lossy media. The accurate calculation of the Green's functions in lossy layered media enables the accurate and efficient modeling of complex structures in lossy semiconductor substrates and new 3D IC structures including through-silicon vias (TSVs).

*Index Terms*—Lossy layered media, spectral-domain Green's functions, surface-wave poles, discrete complex image method (DCIM), pole extraction, Sommerfeld integral.

## I. INTRODUCTION

GREEN'S functions in layered media have been extensively studied during the past several decades. It is necessary to evaluate the Green's functions efficiently in any algorithm based on integral equations (IE) such as the method of moments (MoM), for analyzing multilayer structures such as patch antennas, printed dipoles, high-speed interconnects, microwave and millimeter-wave circuits, etc.

The normal procedures of calculating the Green's functions in layered media start with the spectral-domain Green's functions, which are efficiently constructed based on the generalized reflection and transmission coefficients [1-3]. Then, the spatial-domain Green's functions are evaluated from their spectral-domain counterparts through the well-known Sommerfeld integral (SI). Since SI has the intrinsic property of strong singularity, high oscillation and slow decay, numerical integration is generally time-consuming. Over the years, several methods have been proposed to expedite the calculation of SI [4-7]. Among those methods, discrete complex image method (DCIM) provides closed-form Green's functions in a systematic manner [8], [9].

When applying DCIM, the spherical waves in the spectral domain are approximated in terms of a set of complex exponentials, using the generalized pencil of function (GPOF). Via the Sommerfeld identity, each complex-exponential term in the spectral domain can be easily casted to an analytical term in the spatial domain. However, in order to obtain accurate far-field response, surface-wave poles must be extracted to avoid singularities. Because the surface-wave poles representing cylindrical and lateral surface waves, if approximated with spherical waves, could cause severe deterioration of the DCIM algorithm in the far field.

Although it is a cumbersome step to locate the surface-wave poles for general multiple, especially thick layers [10], significant progress has been achieved and some common methods were well summarized in [11]. For general layered media, contour integrals, first proposed in [12], are usually performed to check the locations of the poles. However, when the surface-wave poles are located close to a branch cut, which is very common for transverse magnetic (TM) waves due to the absence of low cutoff frequency,

the recursive contour integral method becomes less efficient. *Polimeridis et al.* proposed a technique to remove the branch cut using a sine transformation [13]. But this method embodied in the algorithm [14] is not sufficiently efficient for lossy layered media. Moreover, in [11], *Wang et al* proposed to use the Cauchy theorem and criteria to check the locations of the poles. Their criteria improved the accuracy but did not completely solve the errors caused by the branch cut. Consequently, as shown in the numerical examples in Section III, some critical poles were missed in their results (TABLE II in [11]) in lossy media.

Being able to deal with lossy layered media becomes more critical today with the need to characterize and model 3D IC and 3D packaging structures with through-silicon vias (TSVs). Lossy silicon substrate has a significant impact on the electrical performance of these structures. In this paper, a simple yet accurate method is proposed to calculate the contour integral with the presence of a branch cut inside the contour. The algorithm is efficient to remove the effects of the branch cut in general layered media, whether lossless or lossy, and gives good results for searching the poles as well as calculating the residues. The details of the algorithm are presented in Section II, followed by numerical examples to demonstrate the accuracy and the effectiveness of the method in Section III.

## II. FORMULATION

A typical configuration of layered media shown in Fig. 1 is used in the following discussions. The top layer is open (unbounded) and the bottom layer is bounded by a perfect electric conductor (PEC) plane. The spectral-domain Green's functions of such layered media have been well established through equivalent transmission lines with transverse electric (TE) or TM types [2].

When applying DCIM to obtain the analytical spatial-domain Green's functions through the Sommerfled identity, the spectral-domain Green's functions can be decomposed into the form as

$$\widetilde{G} = \widetilde{G}_{pri} + \widetilde{G}_{static} + \widetilde{G}_{sw} + \widetilde{G}_{sp} \tag{1}$$

where $\widetilde{G}$ is a spectral-domain Green's function; $\tilde{G}_{pri}$, $\tilde{G}_{static}$, $\tilde{G}_{sw}$, $\tilde{G}_{sp}$ represent its primary field, quasi-static image, surface-wave and complex image terms, respectively, and

$$\tilde{G}_{pri} = \frac{e^{-jk_z^1|z|}}{2jk_z^1} \tag{2}$$

$$\widetilde{G}_{static} = \frac{A_0}{2jk_z{}^1} \tag{3}$$

$$\tilde{G}_{sw} = \sum_i \frac{2k_{\rho i} Res_i}{k_\rho^2 - k_{\rho i}^2} \tag{4}$$

$$\widetilde{G}_{sp} = \sum_{i=1}^{N_G} a_i e^{-b_i k^1{}_z} \; / 2jk_z^1 \tag{5}$$

where $k_z^1 = \sqrt{k_1^2 - k_\rho^2}$ is the wavenumber in the first open layer, $k_1 = \omega\sqrt{\varepsilon_1\mu_1}$ and $k_\rho$ is the transverse propagation wave number. In addition, $A_0$ is the constant term when $k_\rho \to \infty$; $N_G$ is the number of the complex images; $a_i$ and $b_i$ are the coefficients of the i$^{th}$ complex image; and, $k_{\rho i}$ and $Res_i$ are the i$^{th}$ surface-wave pole and residue. For layered media, only the unbounded layer has branch cut. In any bounded layer, wave could travel at both the $\hat{z}$ and - $\hat{z}$ directions and therefore there is no branch cut. Thus, spherical waves are expanded with regard to the open layer to avoid artificial branch cut [15].

For general lossless media, the pole $k_{\rho i}$ is located along the real axis while $k_{\rho i}$ could be located at any point inside the entire $k_\rho$ plane for lossy media. From the residue theorem, in a simple connected domain $\Omega$ bounded by a Jordan curve $C_r$, the residue of a pole can be obtained through the contour integral in the complex $k_\rho$ plane as

$$Res = \frac{1}{2\pi j} \oint_{C_r} \tilde{G} dk_\rho \tag{6}$$

However, the spectral-domain Green's function $\tilde{G}$ has branch cut in the $k_\rho$ plane, due to the fact that the mode wavenumber for the unbounded layer

$$k_z^1 = \pm\sqrt{k_1^2 - k_\rho^2} \tag{7}$$

is a double-valued complex function. The imaginary part of $k_z^1$ has to be chosen negative to satisfy the radiation condition.

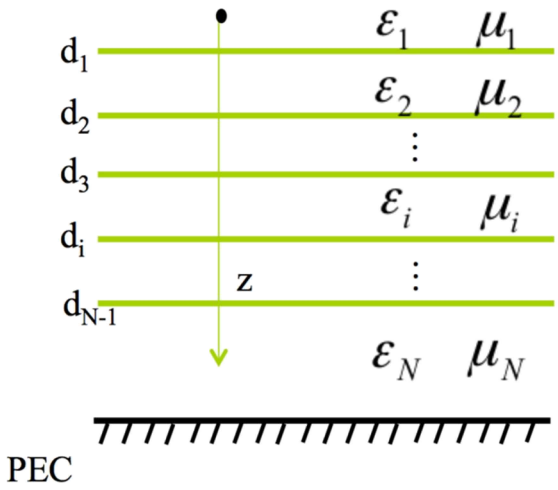


Fig. 1 A typical configuration of layered media with N dielectric layers. The top layer is open and the bottom layer is bounded with a PEC plane.

If the branch cut intersects with the integration path, as illustrated in Fig. 2, the

contour integral (6) will not be zero even if there is no pole inside the closed domain $\Omega$. In other words, (6) is valid to calculate the residue of a pole only when the integration path is within one Riemann sheet of $\tilde{G}$. For this reason, when the location of a pole is close to the branch cut, the algorithm of recursive contour integral [12] fails and the error from the integration path across different Riemann sheets impairs the judgment of pole location as well as the calculation of the residue. Though it is relatively easy to locate any branch point, limiting the contour integral within one Riemann sheet by identifying the entire branch cut is usually cumbersome, especially for layered media.

In order to eliminate the effects of branch cut, we modify (6) and propose the following condition for identifying the location of a pole, with a given error tolerance *e*,

$$|Res| = \left| \frac{1}{2\pi j} \oint_{C_r} (\tilde{G} + \tilde{G}') dk_\rho \right| > e \tag{8}$$

where $\tilde{G}$ and $\tilde{G}'$ could be calculated from (1) when $\mathrm{Im}(k_z^1 < 0)$ and $\mathrm{Im}(k_z^1 > 0)$.

Spurious poles associated with $\tilde{G}'$ would also be selected from (8), thus, we should add one more criterion, as

$$\left| \frac{1}{2\pi j} \oint_{C_r} \tilde{G} dk_\rho \right| > e \tag{9}$$

Conditions (8) and (9), together with the recursive contour integration method [12] or the Cauchy's integral theorem [11], could accurately locate all the poles, no matter how close they are to the branch cut.

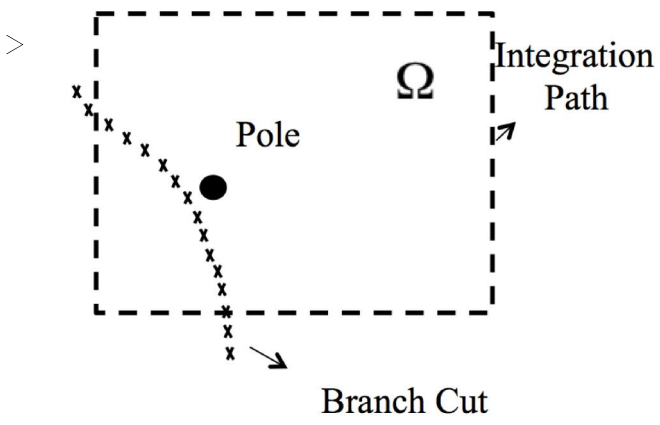


Fig. 2 Contour integration with branch cut intersecting with the integration path.

## III. NUMERICAL RESULTS AND DISCUSSIONS

In this section, we provide numerical examples to demonstrate the accuracy and the effectiveness of the proposed method, for both lossless and lossy layered media. In the implementation of the proposed algorithm, the error tolerance in (8) and (10) is selected as 1e-5. The region for searching the poles is limited within a square centered at the origin with edge length of 2e4 along both the real and imaginary axis directions.

First, the surface-wave poles associated with both TE and TM modes in a single-layer medium with parameters of $\varepsilon_r = 4$, layer thickness $h = 5$ mm and the operation frequency $f = 10$ GHz are studied, same as in [11] and [13]. The Green's function in this example has a single TE-mode pole that is very close to its branch point at $k_\rho = k_0 = 2.0958$. The results from the proposed method are compared with the previously published results in TABLE I. It can be observed that the results from the proposed method are nearly identical with those from [13].

Table I

TE AND TM WAVE POLES IN A SINGLE-LAYER MEDIUM WITH LOSSLESS OR LOSSY DIELECTRIC MATERIAL

| Pole (rad/cm) | | Lossless | tan $\delta$ =0.02 |
|---|---|---|---|
| $\rho_{TM}$ | method in this paper | 3.265300 | 3.2653-j0.0402 |
| | method in [11] | 3.261989 | 3.2620-j0.0401 |
| | method in [13] | --- | 3.2653-j0.0402 |
| $\rho_{TE}$ | method in this paper | 2.223390 | 2.2226-j0.0238 |
| | method in [11] | 2.220789 | 2.2200-j0.0237 |
| | method in [13] | 2.22 | 2.2226-j0.0238 |

Then, surface-wave poles of the Green Function in the same four-layer media with a PEC ground plane as discussed in [11] and [13] are studied. The structure is shown in Fig. 3 and the frequency is 30 GHz. In this example, the surface-wave poles are very close to the branch cut. Direct methods in [12] and [14] failed. In [13], only lossless case was considered since the method is not sufficiently efficient for lossy layered media. And the technique in [11] missed several critical poles for the lossy case as illustrated in Table II.

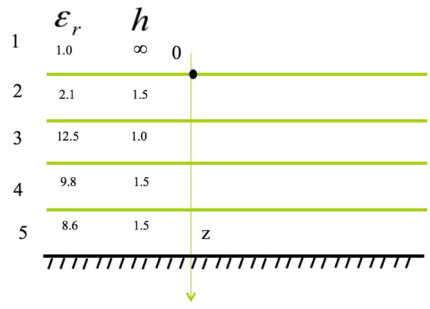


Fig. 3 Configuration of the four-layer media, as illustrated in [11], used as an example.

All the poles obtained from the proposed method are listed in Table II, which also includes the results from [11] and [13]. From the table, it can be observed that in the lossless case the poles extracted by the proposed method match with those from [13], but are slightly different than those from [11]. However, for the lossy case, the proposed method identified more poles for both the TE and TM modes than the method in [11]. The extra poles identified from the proposed algorithm are not due to a higher error tolerance, because the residues of some of these poles are sufficiently large and they dominate the surface-wave behavior in the far field. To further verify the accurate locations of these poles in the lossy media, contour plots in the complex $k_\rho$ plane are shown in Fig. 4 and Fig.5. Due to the space limitation of the paper, only several significant poles for the TM waves are shown. But all the poles identified by the proposed method are verified to be true and accurate.

Table II

TE AND TM WAVE POLES IN FOUR-LAYER MEDIA WITH LOSSLESS OR LOSSY DIELECTRIC MATERIALS

| Pole (rad/cm) | | Lossless | tan $\delta$ | |
|---|---|---|---|---|
| $\rho_{TM}$ | | 8.6019 | 7.915-j2.75 | 4.477-j1.495 |
| | | 16.1638 | 16.32-j2.308 | 1.528-j19.04 |
| | method in this paper | 18.8632 | 18.95-j1.993 | 0.420-j28.45 |
| | | | 0.733-j38.32 | 0.484-j46.89 |
| | | --- | 0.175-j56.21 | 0.383-j63.31 |
| | | | 0.265-j80.49 | 0.149-j87.91 |
| | method in [11] | 8.5844 | 7.8894-j2.7340 | |
| | | 16.1478 | 16.3122-j2.3076 | |
| | | 18.8498 | 18.9407-j1.9917 | |
| | method in [13] | 8.6019 | --- | |
| | | 16.1638 | --- | |
| | | 18.863 | --- | |
| $\rho_{TE}$ | method in this paper | 6.2894 | 4.43867-j3.8411 | |
| | | 14.8323 | 15.0099-j2.4616 | |
| | | 19.1407 | 19.2472-j2.1411 | |
| | method in [11] | 6.2841 | --- | |
| | | 14.8151 | 14.9927-j2.4607 | |
| | | 19.1259 | 19.2322-j2.1396 | |
| | method in [13] | 6.2893 | --- | |
| | | 14.8323 | --- | |
| | | 19.1407 | --- | |

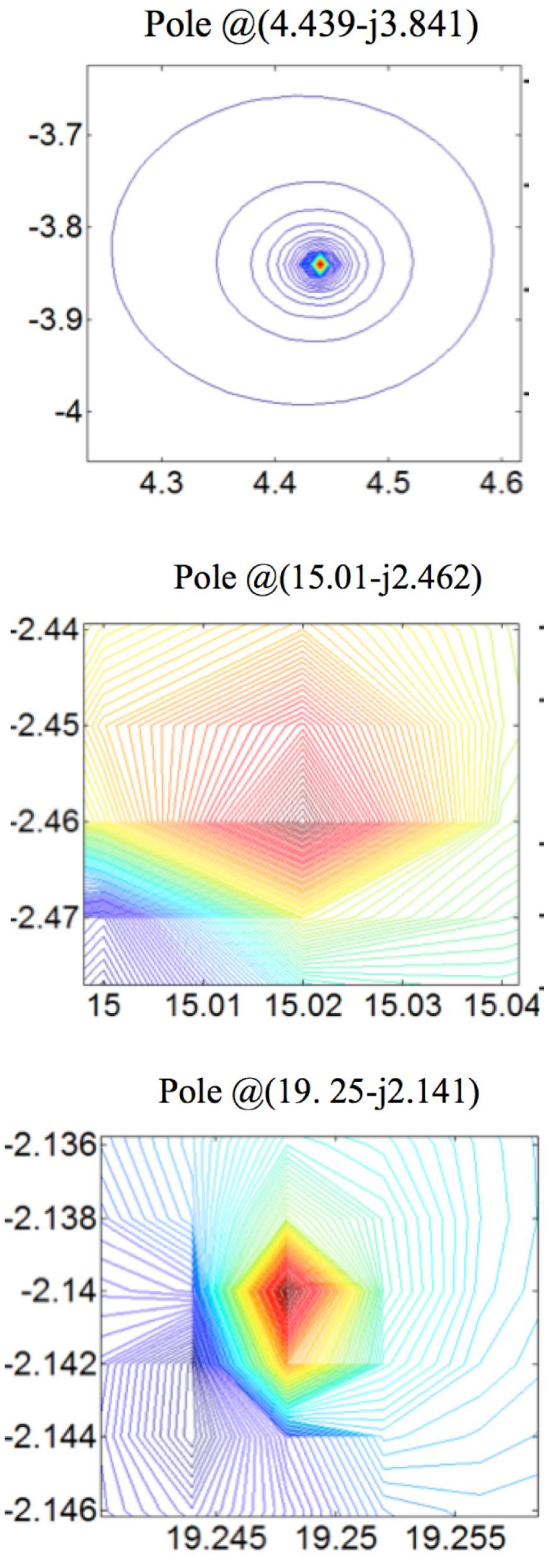


Fig. 4 Contour plots of the magnitude of the normalized TE waves in the complex kp plane for the lossy case. The three most significant poles are plotted. The locations of the poles match well with those extracted from the proposed method listed in Table II.

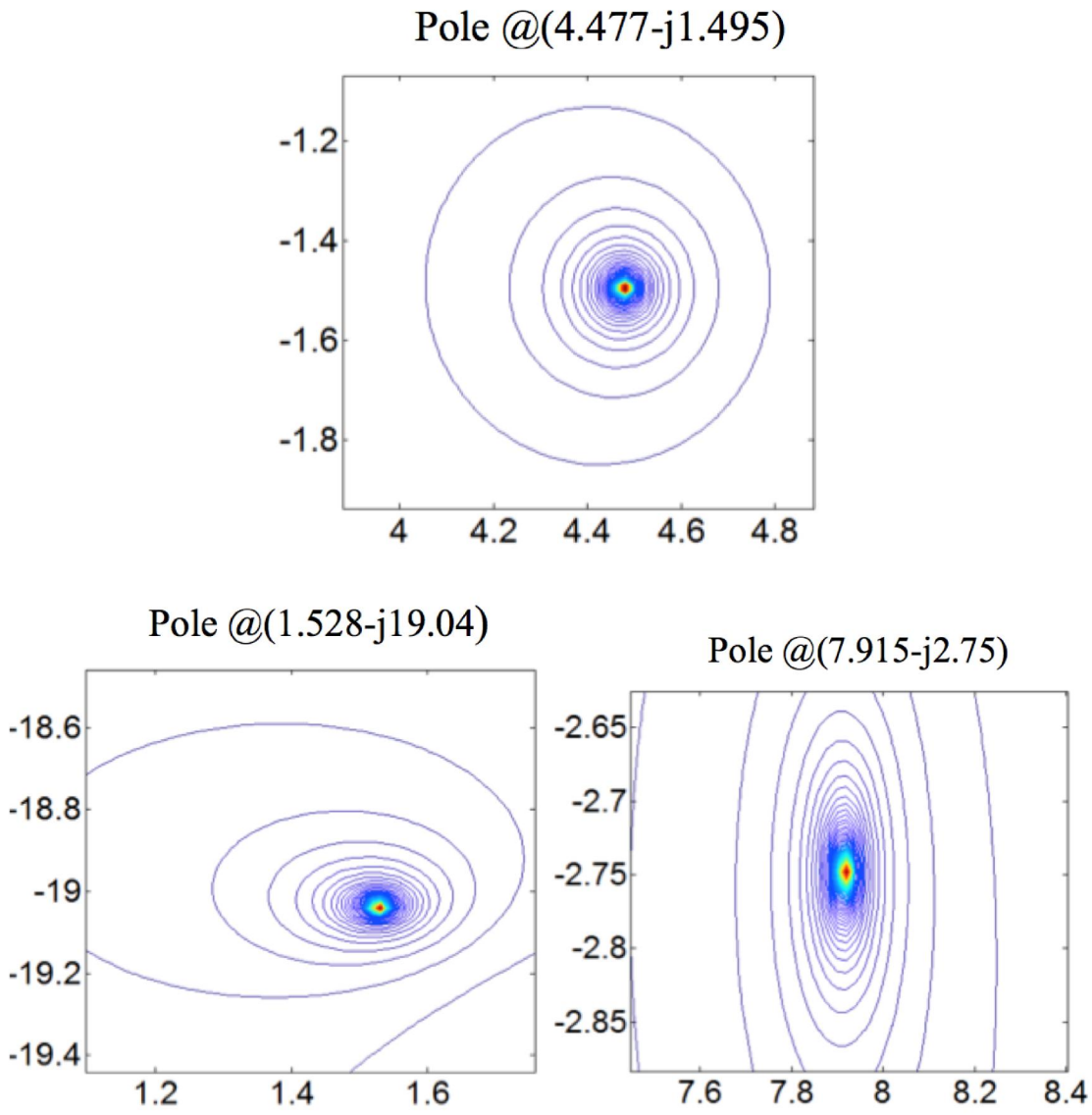


Fig. 5 Contour plots of the magnitude of the normalized TM waves in the complex $k_p$ plane for the lossy case. The remaining three significant poles are plotted. The locations of the poles match well with those extracted from the proposed method listed in Table II.

The proposed method could be generalized to calculate the residues using contour integral with the presence of any number of branch cuts. Suppose a total number of $N$ branch cuts intersecting with the integration path, the computational time of locating the poles increases to $2^N$. Fortunately, in general layered media, the maximum number of

branch cuts associated with unbounded media that could impact the contour integral for locating poles is only 2. Thus, the pole extraction algorithm proposed in this paper can still be embodied into DCIM to improve its efficiency with a negligible increase of computational time.

## IV. CONCLUSION

A robust and automatic method to extract the surface-wave poles of the spectral-domain Green's functions for general layered media is proposed. Both lossless and lossy dielectric materials can be effectively handled. The proposed method can accurately identify the surface-wave poles located close to the branch cut. Through the numerical examples and the comparisons with the previously published results, the proposed approach has been demonstrated more effective and accurate to handle lossy layered media.

## REFERENCES

[1] W. C. Chew, "Wave and Fields in Inhomogeneous Media," IEEE Press, NJ, 1995.

[2] K. Michalski, and J. Mosig, "Multilayered media green's functions in integral equation formulations," IEEE Trans. Antennas and Propagation, vol. 45, no.3, Mar. 1997.

[3] J. R. Mosig, "Arbitrarily shaped microstrip structures and their analysis with a mixed potential integral equation," IEEE Trans. Microwave Theory Tech., vol. 36, pp. 314-323, Feb. 1988

[4] B. Hu and W. C. Chew, “Fast inhomogeneous plane wave algorithm for electromagnetic solutions in layered medium structures—2D case,” Radio Sci., vol. 35, no. 1, 2000.

[5] K. A. Michalski, “Extrapolation methods for Sommerfeld integral tails,” IEEE Trans. Antennas Propagat., vol. 46, pp. 1405–1418, Oct. 1998.

[6] Q.-H. Liu and W. C. Chew, “Application of the conjugate gradient fast Fourier transfer method with an improved fast Hankel transform algorithm,” Radio Sci., vol. 29, pp. 1009–1022, July–Aug. 1994.

[7] W. Cai and T. Yu, “Fast calculation of Dyadic Green function for electromagnetic scattering in a multilayered medium,” J. Comput. Phys., Nov. 1999.

[8] C. Y. Chow, J. Yang, D. Fang, G. E. Howard, “A closed-form Spatial Green’s Function for the Thick Microstrip Substrate”, IEEE Trans. Microwave Theory and Techniques, vol. 39, no 3, Mar. 1991.

[9] M. I. Aksun, “A robust approach for the derivation of closed-form Green’s functions,” IEEE Trans. Microwave Theory Tech., vol. 44, pp. 651–658, May 1996.

[10]V. Okhmatovski, A. Cangellaris, “A new technique for the derivation of closed-form electromagnetic green’s function for unbounded planar layered media,” IEEE Trans. Antennas and Propagation, vol. 50, no. 7, July. 2002.

[11]D. Wang, E. Yung, R. Chen, J. Bao, “A New Method for Locating the Poles of Green’s Functions in a Lossless or Lossy Multilayered Medium”, IEEE Trans. Antennas and Propagation, Vol 58, No, 7, July 2010.

[12]L. Feng, and J. Jin “Discrete complex image method for green’s functions of general multilayer media,” IEEE Microwave and Guided Wave Letters, Vol. 10, No 10, Oct. 2000.

[13]A. Polimeridis, T. Yioultsis, T. Tsiboukis, “An Efficient Pole Extraction Technique for the Computation of Green’s Functions in Stratified Media Using a Sine Transformation,” , IEEE Trans. Antennas and Propagation, Vol 55, No, 1, Jan 2007.

[14] S. A. Teo, S. T. Chew, and M. S. Leong, “Error analysis of the discrete complex image method and pole extraction,” IEEE Trans. Microw. Theory Tech., vol. 51, pp. 406–413, Feb. 2003.

[15]R. Kipp and C. Chan, “Complex image method for sources in bounded regions of multilayer structures,” IEEE Trans. Microw. Theory Tech., vol. 42, pp. 860–865, May. 1994.

[16]A. Bhattacheryya, “Characteristics of space and surface waves in a multilayered structure”, IEEE Trans. on Antennas and Propagation, Vol. 38, No. 8, Aug. 1990.

[17]Rodriguez-Berral, R., Mesa, F.. Medina, F., "Enhanced implementation of the complex images method to study bound and leaky regimes in layered planar printed lines," IEEE Transactions on Microwave Theory and Techniques, vol.52, no.2, pp.709-720, Feb. 2004.

# III. MODELING OF COPLANAR WAVEGUIDE ON 2.5D SILICON INTERPOSER

Siming Pan and Jun Fan

*Abstract*— A new equivalent circuit model is proposed in this paper to model CPW structure on silicon interposer. The 2D lossy metal-isolator-semiconductor (MIS) coplanar waveguide (CPW) is represented by simple RLGC circuit. The shunt admittance of the equivalent circuit model is derived rigorously based on partial equivalent element circuit (PEEC) in layered media. The silicon effects on series inductance have also been studied by employing the modified green functions with semiconductor images at a complex distance from spectrum domain analysis. It is also demonstrated in the paper that the silicon effects on series impedance can be neglected in conventional CMOS processes. A test 2.5 silicon interposer is fabricated to validate the effectiveness of the model. The presented circuit model shows good correlations with full-wave simulations as well as the measurements on the test interposer.

*Index Terms*— On-chip interconnect, silicon interposer, through-silicon-via (TSV), partial equivalent element circuit (PEEC), complex image theory, signal integrity.

## I. INTRODUCTION

Recently 3D integration explores a new solution to keep pace with Moore's Law for the semiconductor industry. Nowadays the performance of the integrated circuits is highly depends on the interconnect designs as the interconnect delay has exceeded the gate

switching delay. On the other hand, the total number of Input / Output (IO) and Power / Ground (PG) terminals keep increasing due to requirements of rapid advance in integration density and performance [1, 2]. Design rules of the wiring and bump pitch on the substrate continue to shrink, thus, passive interposer using silicon substrate with TSVs has emerged as a reliable solution to connect with chips using smaller interconnects [3]. Since multiple active ICs from different technologies can be mounted over the silicon interposer, silicon interposer platform guarantees heterogeneous system-in- package (SIP) solutions in a small form-factor [4].

Due to the increase in operating frequencies, the performance of signal links could be a critical problem to impact signal integrity. The previous lumped resistance-capacitance (RC) models may not be suitable to accurately characterize signal delay and loss of the interconnect on the silicon interposer, due to relatively long signal transmission in silicon environment and high operation frequency [5, 6]. Coplanar waveguide (CPW) transmission lines are commonly realized in the conventional CMOS processes for global power and signal routing. In order to evaluate the electrical behaviors of the broad-band transmission line for CPW structure on lossy silicon substrate, a variety of numerical techniques and modeling methodology was summarized in [7]. Most of the proposed models clarify three different modes of wave propagations for MIS, originally reported by H. Hasegawa [8]. They proposed “skin-effect”, “slow-wave” and “quasi-TEM” mechanism according to the comparison between operation frequency and silicon relaxation frequency. J. Aguilera developed a quasi-static approach in spectral domain for layered isolator-semiconductor substrate [9]. But the conductor losses can be dominant for the on-chip MIS structure [10]. So a quasi-TM model is extended to include nonperfectly

metallic conductors in [11], where G. Plaza proposed a quasi-TM model by carefully defining the meaning of voltage and current and used the combination of method of lines (MoL) and method of moments (MoM) to solve the integral equation. This work was extended to include multi-conductor case in [12]. Distributed frequency-dependent resistance, inductance, conductance and capacitance (RLGC) transmission line model was also extracted for integrated circuit CPW based on quasi-TEM field in [13, 14]. However, a simple circuit model with frequency-independent elements is always desired for fast spice-compatible simulations in time domain. The circuit model proposed in Fig. 4 in [15] was widely used and various approaches were developed to calculate the circuit elements for this circuit topology. V. Milanovic provided an equivalent circuit model for CPW with deep doping substrate and compared with on-wafer measurements. But the derivations of the topology and elements of the equivalent circuit are not rigorous, which results in more capacitance shown in the measurements than that from the model [16]. Another equivalent circuit model was proposed by K. Kang for wideband applications but empirical formulas were used to fit the elements in the model [17].

In this paper, we proposed a new circuit topology for MIS CPW structures based on partial element equivalent circuit (PEEC) [18, 19]. As demonstrated in [20, 21], the per-unit-length capacitance and inductance for this type of slow-wave transmission line can be calculated separately. While the effective resistance is mostly dominate by the skin loss of the conductor rather than the loss from eddy current in silicon, the calculations of inductance and resistance could simply use the similar methods mentioned in [19]. The equivalent circuit model related to capacitance and conductance in inhomogeneous regions are derived through PEEC method combined with complex image theory. The proposed

method assumes the ratio between trace space and width should not be too small, which is valid in most conventional CMOS processes due to design rules restrictions. The error induced by this method is also analyzed for different geometrical constrains.

The paper is organized as followings, in Section II, we derive an equivalent circuit model with frequency-independent elements for CPW structure on silicon interposer. In Section III, circuit model for TSV is reviewed first then we combined CPW and TSV model together. Validations of the models are demonstrated in Section IV through full-wave simulations and on-wafer measurements on a test silicon interposer. We conclude our work in Section V.

## II. EQUIVALENT CIRCUIT MODEL FOR CPW STRUCTURE ON SILICON INTERPOSER

Fig. 1 shows a typical geometry of coplanar waveguide on the silicon interposer. Through quasi-static analysis, the electrical properties of the CPW structure can be accurately determined by per-unit-length impedance and admittance parameters, as demonstrated in [22]. Though the total shunt admittance for on-chip CPW is frequency dependent in a wide frequency range, it could be represented by frequency-independent capacitance and conductance with appropriate circuit topology. Meanwhile, in today's commonly used CMOS processes, the resistivity of silicon substrate is generally less than 1 Ω·cm. Thus, the effective substrate resistance is relatively small compared to skin-effect loss. The proposed circuit model simply uses the impedance from CPW in homogenous media to account for serial impedance elements of on-chip CPW structures.

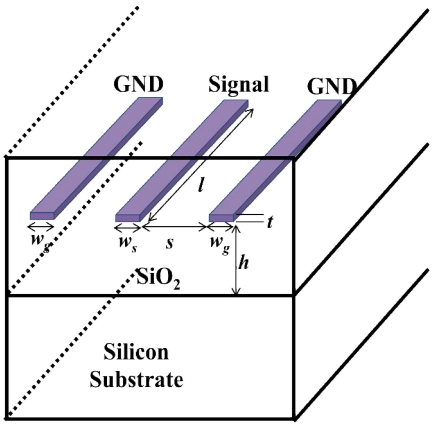


Fig. 1 Coplanar waveguide on silicon interposer

A. Circuit Model for Shunt Admittance Parameters

The so called short circuit capacitance matrix [23] for the CPW structure in dielectric media is defined as,

$$\begin{bmatrix} Q_1 \\ Q_2 \end{bmatrix} = \begin{bmatrix} C_{s11} & C_{s12} \\ C_{s21} & C_{s22} \end{bmatrix} \begin{bmatrix} \Phi_1 \\ \Phi_2 \end{bmatrix}, \tag{1}$$

where $\mathbf{C_s}$ is the short circuit capacitance matrix for signal and ground conductors, $Q_1$, $Q_2$, $\Phi_1$, $\Phi_2$, are the total charges and potentials on signal and ground conductors, respectively.

The lumped equivalent capacitance between signal and ground conductors can be easily evaluated by

$$C_{lump} = C_{s21} = \frac{Q_2}{\Phi_1} \text{ when } \Phi_2 = 0\,. \tag{2}$$

From the integral solution of Maxwell's equations, the relationship between the charge density and the potential is given as [24]

$$\Phi(\mathbf{r}) = \int G_c(\mathbf{r}, \mathbf{r}')q(\mathbf{r}')ds'\,. \tag{3}$$

where $q$ is the charge density on the conductor surfaces, and $G$ is the Green's function. $\mathbf{r}$

and **r'** are the position vectors of the source and observation points.

If the charge uniformly distributes on the surface of the conductors, (3) becomes

$$\Phi(\mathbf{r}) = \sum_{i=1,2} \frac{Q_i}{S_i} \int G_c(\mathbf{r}, \mathbf{r}')ds', \tag{4}$$

where $S_1$, $S_2$ represent the total surface areas for signal and ground conductors.

Next, apply Galerkin's approach to match the potential for signal and ground with averaging (4) over their surface, we can obtain [24]

$$\Phi_{j=1,2} = \sum_{i=1,2} Q_i ps_{ij} \tag{5}$$

where

$$ps_{ij} = \frac{1}{S_j S_i} \int_{S_i} \int_{S_j} G_c(\mathbf{r}, \mathbf{r}')ds'ds. \tag{6}$$

For on-silicon CPW structure, inhomogeneous $SiO_2$-Silicon media are usually involved. The Green's function for this layered media can be derived from the free space Green's function using the image theory **Error! Reference source not found.**. Since both signal and ground conductors are in the $SiO_2$ layer, source and observation points are in the same media. Thus, the Green's function for CPW structure in $SiO_2$-Silicon media shown in Fig. 2 can be written as

$$G_c(\mathbf{r}, \mathbf{r}') = \frac{1}{4\pi} \frac{1}{|\mathbf{r} - \mathbf{r}'|} \frac{1}{\varepsilon_{sio_2}} + \frac{1}{4\pi} \frac{1}{|\mathbf{r} - \mathbf{r_{im}}'|} \frac{1}{\varepsilon_{sio_2}} \frac{\varepsilon_{sio_2} - \varepsilon^c_{si}}{(\varepsilon_{sio_2} + \varepsilon^c_{si})} \tag{7}$$

where $\mathbf{r_{im}}'$ is the position vectors of the image of observation points. $\varepsilon_{sio_2}$ is the permittivity of $SiO_2$.

$$\varepsilon^c_{si} = \varepsilon_{si} + \frac{\sigma_{si}}{j2\pi f}. \tag{8}$$

$\varepsilon_{si}$ and $\sigma_{si}$ are permittivity and conductivity of the silicon, respectively.

In order to develop an intuitive physics-based circuit model, we assume charge distributes uniformly on the 2-D surface of signal and ground conductors when we first decompose the circuit elements from rigorous PEEC definition. This assumption will be revised and discussed later in Section IV.

Consider signal and ground conductors as two uniform cells and apply (7), the **Ps** matrix defined in (6) becomes

$$\mathbf{Ps} = \begin{bmatrix} a_{ss}\dfrac{1}{\varepsilon_{sio_2}} + a_{ss'}\dfrac{1}{\varepsilon_{sio_2}}\dfrac{\varepsilon_{sio_2}-\varepsilon^c{}_{si}}{(\varepsilon_{sio_2}+\varepsilon^c{}_{si})} & a_{sg}\dfrac{1}{\varepsilon_{sio_2}} + a_{sg'}\dfrac{1}{\varepsilon_{sio_2}}\dfrac{\varepsilon_{sio_2}-\varepsilon^c{}_{si}}{(\varepsilon_{sio_2}+\varepsilon^c{}_{si})} \\ a_{sg}\dfrac{1}{\varepsilon_{sio_2}} + a_{sg'}\dfrac{1}{\varepsilon_{sio_2}}\dfrac{\varepsilon_{sio_2}-\varepsilon^c{}_{si}}{(\varepsilon_{sio_2}+\varepsilon^c{}_{si})} & a_{gg}\dfrac{1}{\varepsilon_{sio_2}} + a_{gg'}\dfrac{1}{\varepsilon_{sio_2}}\dfrac{\varepsilon_{sio_2}-\varepsilon^c{}_{si}}{(\varepsilon_{sio_2}+\varepsilon^c{}_{si})} \end{bmatrix} \tag{9}$$

where $\begin{bmatrix} a_{ss} & a_{sg} \\ a_{sg} & a_{gg} \end{bmatrix}$ is the **Ps** matrix purely related to the geometry of signal and ground conductors in the homogenous air, as shown in Fig. 2 (a). $a_{ss'}, a_{sg'}, a_{gg'}$ can be calculated using (6) with free space Green function in air between the original conductor and its image, as shown in Fig. 2 (b), (c) and (d), respectively. For 2-D rectangular conductors in homogenous media, all the coefficients in (9) can be evaluated analytically [24], [26].

The shunt admittance between the signal and ground conductors in $SiO_2$-Silicon media can be obtained through equation (9), as

$$Y_{total} = \frac{1}{(a_{ss}+a_{gg}-2a_{sg})\dfrac{1}{\varepsilon_{sio_2}} + (a_{ss'}+a_{gg'}-2a_{sg'})\dfrac{1}{\varepsilon_{sio_2}}\dfrac{\varepsilon_{sio_2}-\varepsilon^c{}_{si}}{(\varepsilon_{sio_2}+\varepsilon^c{}_{si})}} \tag{10}$$

By exploiting the pair capacitance between the two conductors from four configurations in Fig. 2, we can write the equivalent admittance in (10) as

$$Y_{total} = \frac{1}{b_1\dfrac{1}{\varepsilon_{sio_2}} + b_2\dfrac{1}{(\varepsilon_{sio_2}+\varepsilon^c{}_{si})}} \tag{11}$$

where

$$b_1 = (b_{(a)} + \frac{b_{(b)}}{2} + \frac{b_{(d)}}{2} - b_{(c)}) \tag{12}$$

$$b_2 = (2b_{(c)} - b_{(b)} - b_{(d)}) \tag{13}$$

and

$$b_{(i)} = 1 / C_{(i)} \qquad i = a, b, c, d \tag{14}$$

$C_{(i)}$ is the pair capacitance between two groups of conductors in homogenous media in Fig. 2 (i).

Finally, the equivalent circuit model for the shunt admittance between signal and ground CPW on silicon can be derived based on (11) and shown in Fig. 3. And the capacitance and conductance elements can be expressed as

$$C_{1\_sio_2} = \varepsilon_{sio_2} / b_1 \tag{15}$$

$$C_{2\_sio_2} = \varepsilon_{sio_2} / b_2 \tag{16}$$

$$C_{2\_si} = \varepsilon_{si} / b_2 \tag{17}$$

$$G_{2\_si} = \sigma_{si} / b_2 \tag{18}$$

The elements in the equivalent circuit model are directly related to physical geometry. In the design of on-chip interconnects, smaller conductance is usually desired to reduce loss for signal transition. In order to reduce $G_{2\_si}$, the capacitance from the configuration in Fig. 3(c) needs to be increased while the capacitance of the geometry in Fig. 3(b) and (d) needs to be decreased. Thus, to reduce the spacing between signal and

GND conductors and to increase the vertical distance between conductors and silicon will help to reduce loss caused by shunt conductance.

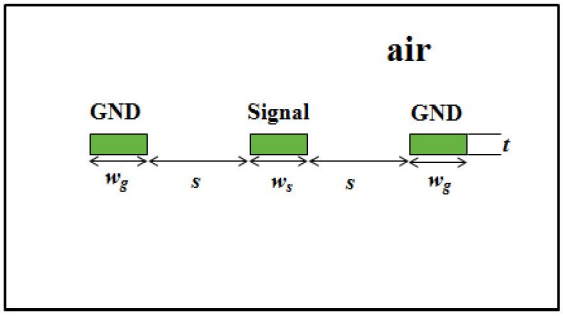


(a)

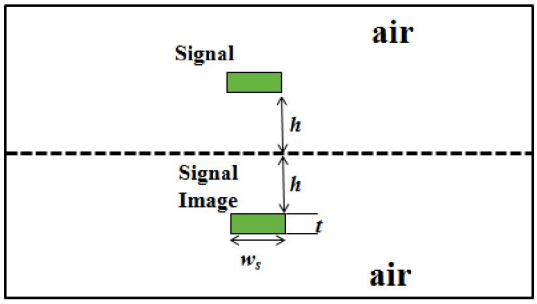


(b)

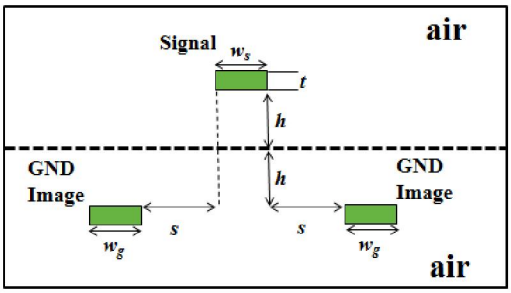


(c)

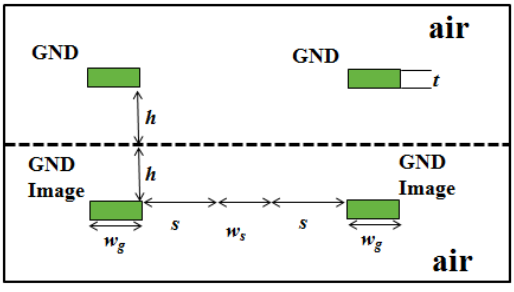


(d)

Fig. 2 Geometry to calculate the coefficients in the **Ps** matrix in Equation (9): (a) $a_{ss}$, $a_{sg}$, $a_{gg}$ (b) $a_{ss'}$ (c) $a_{sg'}$ (d) $a_{gg'}$

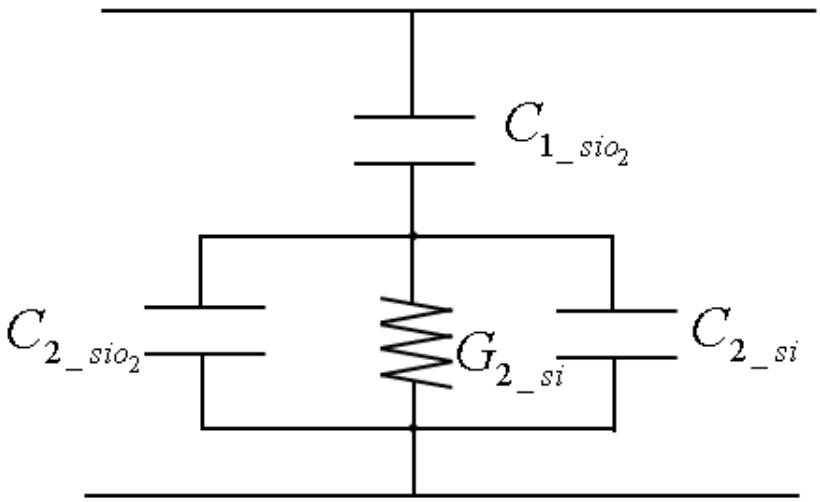


Fig. 3 Equivalent circuit model for the shunt admittance between signal and ground from rigorous derivation of PEEC method

B. Silicon Effects on Series Impedance Parameters

The silicon can affect the current distribution of the on-chip CPW structure due to the eddy currents in the substrate induced by the time varying magnetic field. For a line current above a semi-infinite silicon substrate, the solution of vector magnetic potential can be expressed in term of the 2-D Green's function as

$$A_z(\mathbf{r}) = \int G_l(\mathbf{r},\mathbf{r}')J_z(\mathbf{r}')ds' . \tag{19}$$

With the coordinates defined in Fig. 4, the spatial domain Green's function can be expressed with its spectral counterpart through well-known Sommerfeld integral, as

$$G_l^{\,A}(\Delta\rho,z,z') = \frac{1}{4\pi}\int_{-\infty}^{+\infty}\widetilde{G}_l^{\,A}(k_\rho,z,z')H_0^{(2)}(k_\rho\Delta\rho)k_\rho dk_\rho \tag{20}$$

where $H_0^{(2)}$ is the zero order Hankel function of the second kind.

$$\Delta\rho = \sqrt{(x-x')^2 + (y-y')^2} \tag{21}$$

The spectrum-domain Green's function in the SiO2 region in Fig. 4 can be represented as [28]:

$$\widetilde{G}_l^{\,A} = \frac{\mu_0}{4\pi}\frac{1}{j2k_{z\_sio_2}}(e^{-jk_{z\_sio_2}(z-z')} + R_{TE}e^{-jk_{z\_sio_2}(z+z')}) \tag{22}$$

where

$$R_{TE} = -\frac{r^{TE} + e^{-jk_{z\_si}h_{si}}}{1 + r^{TE}e^{-jk_{z\_si}h_{si}}} \tag{23}$$

$$r_{TE} = -\frac{k_{z\_sio_2} - k_{z\_si}}{k_{z\_sio_2} + k_{z\_si}} \tag{24}$$

$$k_{z\_sio_2}{}^2 = k_{sio_2}{}^2 - k_\rho{}^2 \tag{25}$$

$$k_{z\_si}{}^2 = k_{si}{}^2 - k_\rho{}^2 \tag{26}$$

As the impedance of the CPW can be accurately determined over a wide frequency range beyond 10 GHz by quasi-static analysis, only the quasi-static image is considered in (22) by setting the frequency to approach DC, thus, for the electrical dipole in $\rho$ direction, as shown in Fig. 4,

$$k_{z\_sio_2} = jk_\rho \tag{27}$$

$$k_{z\_si} = (-j\omega\sigma - k_\rho{}^2)^{0.5} \tag{28}$$

Assume an image exist in the distance of $z'+h_{complex}$

$$R_{TE} = R_{TE0} = -\frac{r^{TE} + e^{-j2k_{z\_si}h_{si}}}{1 + r^{TE}e^{-j2k_{z\_si}h_{si}}} = -e^{-jk_{z0}h_{complex}} \tag{29}$$

Note that $k_\rho \to 0$ means no variations in the $\rho$ direction, thus, the complex distance can be calculated as by substituting (27), (28) to (29) and yields

$$h_{complex} = \lim_{k_y \to 0} \frac{-R_{TE0}}{-jk_{z\_sio2}} = \frac{2}{\delta}\tanh(\delta h_{si}) \tag{30}$$

where

$$\delta = \sqrt{j\omega\mu_{si}\sigma_{si}} \tag{31}$$

If there is no ground at the bottom, the complex distance can be obtained as

$$d_{complex} = \lim_{h_{si} \to 0} h_{complex} = \frac{2}{\delta} \tag{32}$$

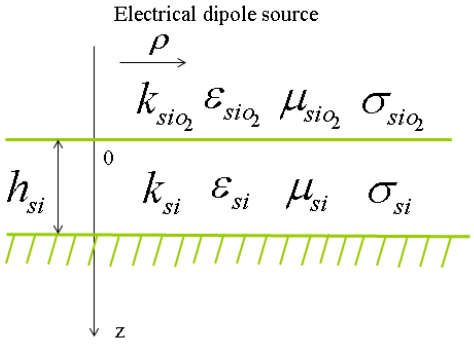


Fig. 4 Geometry and coordinates of layered Si-$SiO_2$ Media

Since in silicon interposer, the thickness of silicon is much larger than it of $SIO_2$, the spatial domain Green's function in $SiO_2$ region without ground plane can be expressed as the vector magnetic potential due to original line current sources and its complex image, as

$$G_l(\mathbf{r},\mathbf{r}') = G_{l\_air}(\mathbf{r},\mathbf{r}') + G_{l\_si}(\mathbf{r},\mathbf{r}') \tag{33}$$

where

$$G_{l\_air}(\mathbf{r},\mathbf{r}') = \frac{\mu_0}{4\pi}\frac{1}{|\mathbf{r}-\mathbf{r}'|} \tag{34}$$

$$G_{l\_si}(\mathbf{r},\mathbf{r}') = \frac{\mu_0}{4\pi}\frac{1}{|\mathbf{r}-\mathbf{r}_{\mathbf{im\_complex}}'|} \tag{35}$$

$\mathbf{r}_{\mathbf{im\_complex}}$' is the position vectors of the complex image of observation points, as shown in Fig. 5. The mirror distance between the original and complex image points is

$$d = 2h + (1 - j)\delta \tag{36}$$

and

$$\delta = \frac{1}{\sqrt{\pi f \mu_0 \sigma_{si}}} \tag{37}$$

The per-unit-length partial inductance of the CPW structures on silicon substrate then can be obtained as

$$L_{mn} = \frac{1}{A_m A_n} \int_{A_m} \int_{A_n} G_l(\mathbf{r}, \mathbf{r}') dA_m dA_n \tag{38}$$

where $A_m$ and $A_n$ are cross-sectional areas of two filaments, in which current distribution varies very little. If

$$\delta >> \max(h, w, t), \tag{39}$$

The partial inductance in equation (25) can be approximate to

$$L_{mn} \approx \frac{1}{A_m A_n} \int_{A_m} \int_{A_n} G_{l\_air}(\mathbf{r}, \mathbf{r}') dA_m dA_n - j\frac{\mu_0}{4\pi\delta} \tag{40}$$

The impedance matrix for filaments is defined by partial inductance with self-resistance, as

$$\mathbf{Z} = \mathbf{R} + j\omega\mathbf{L} \tag{41}$$

where **R** is the DC resistance matrix that only contains diagonal elements. Substitute (40) into (41), the impedance for conductors in $SiO_2$-Silicon layer could be represented as,

$$\mathbf{Z}_{sio_2-si} = \mathbf{Z}_{air} + \frac{\omega\mu_0}{4\pi\delta} \cdot \mathbf{1}_{N\times N} \tag{42}$$

$N$ is the total numbers of filaments and $\mathbf{1}_{N\times N}$ is an $N \times N$ matrix with all the elements equal to 1.

The series impedance in the equivalent circuit model with $SiO_2$-Silicon media is the loop impedance and therefore can be calculated as

$$Z_s = \mathbf{B}(\mathbf{A}\mathbf{Z}_{sio_2-si}^{-1}\mathbf{A}')\mathbf{B}' \tag{43}$$

where

$$\mathbf{A} = \begin{bmatrix} \mathbf{I}_{N_s+1} & 0 \\ 0 & \mathbf{1}^c_{N_g-1} \end{bmatrix}, \qquad \mathbf{B} = \begin{bmatrix} 1 & -1 \end{bmatrix}. \tag{44}$$

$N_s$, $N_g$ are the numbers of filaments for sigal and ground conductors, respectively. $\mathbf{I}_{N_s+1}$ is the identity matrix and $\mathbf{1}^c_{N_g-1}$ is a column vector with all the elements equal to 1.

As $\mathbf{Z}_{air}$ is a symmetric and

$$\text{rank}\left(\frac{\omega\mu_0}{4\pi\delta}\cdot\mathbf{1}_{N\times N}\right) = 1, \tag{45}$$

the series impedance in (43) can be simplified to [27]

$$Z_s = \mathbf{B}(\mathbf{A}\mathbf{Z}_{air}^{-1}\mathbf{A}')\mathbf{B}' \tag{46}$$

Therefore, if equation (39) is satisfied, the series impedance in (42) for CPW structure in $SiO_2$-Silicon media can be simply calculated as the impedance of the same conductors in homogenous media. In today's conventional CMOS process, the conductivity of silicon is usually large than $1\Omega\cdot cm$. In the frequency of interests up to 50 GHz, $\delta$ is much larger than the dimensions of the interconnects. Thus, the eddy current in the silicon substrate generally has little effects on the series impedance in the equivalent circuit model.

Fig. 6 shows the series resistance and inductance for the CPW structures in Fig. 1 with different media. The simulations were performed using commercial electromagnetic field solver based on finite element method (FEM). In all the examples as well as the CPW structures fabricated on the test interposer using in this paper, the widths $w_s$ and $w_g$ of the signal and ground traces are all *10* um. The spacing between traces is also *10* um. The thickness *t* of the metal is *1* um. The height of the metal layer to the silicon substrate *h* is *0.5* um. The results in Fig. 6 compare the per-unit-length impedance with different conductivity of the silicon and the impedance with homogenous air. The deviations among the impedance in Fig. 6 were less than 1%, which demonstrates that the series impedance of on-chip CPW structure can be simply obtained from the impedance of same structure in homogenous media.

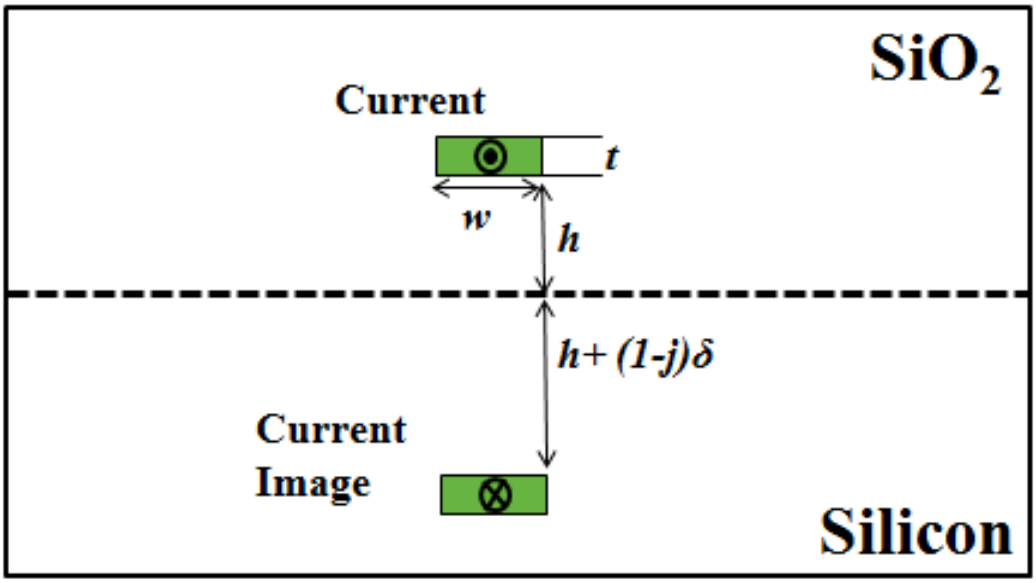


Fig. 5 Complex image of line current source in $SiO_2$-Silicon media. The current flows in the opposite direction in the original and image lines.

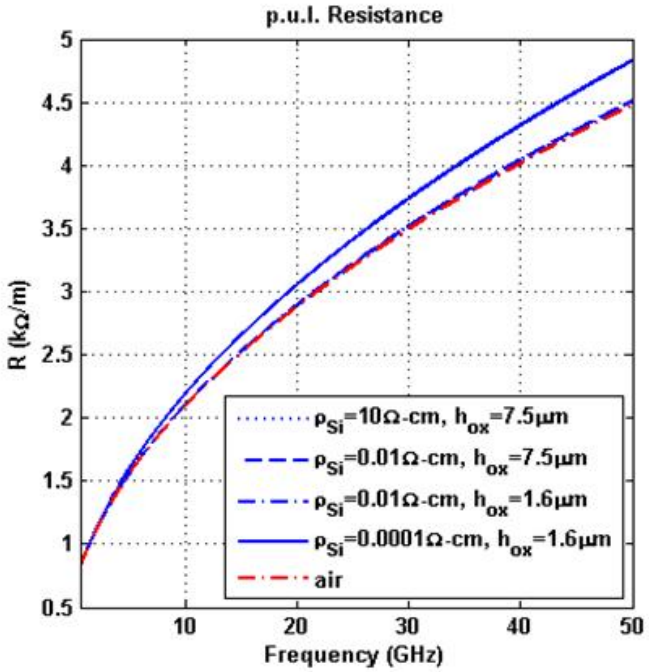


(a)

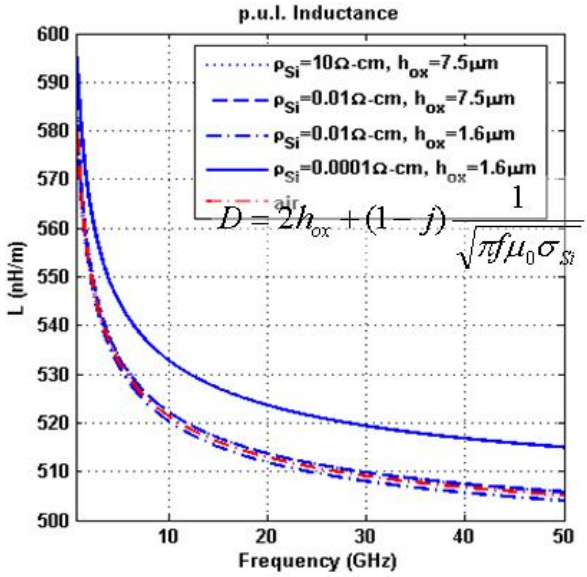


(b)

Fig. 6 Comparisons of the series impedance for on-chip CPW structures with different conductivity of silicon substrate. The impedance of the same CPW structures in homogenous air is set as reference. Only minor differences exist between the impedance in $sio_2$-silicon media and that in homogenous air.

## III. RESULTS AND DISCUSSION

### A. Discussion on Circuit Model for Shunt Admittance

To validate the proposed circuit model for the on-chip CPW in Fig. 1, the admittance from the circuit model are compared with that obtained from full-wave simulator based on FEM in Fig. 7. The conductivity of silicon is $10\,\Omega\cdot cm$. All the dimensions are the same as the example mentioned in Section II.

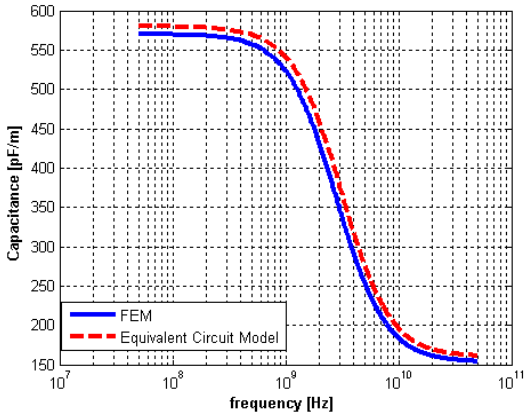


(a)

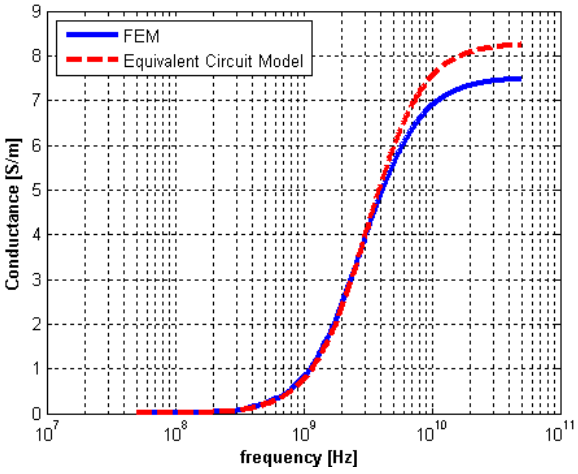


(b)

Fig. 7 Shunt admittance obtained from our model is compared with simulated results using FEM: (a) capacitance (b) conductance

In the derivation of the equivalent circuit model for shunt admittance of on-chip CPW structure, we assumed the charge uniformly distribute on the surfaces of the conductors and ignored the proximity effect. Theoretically, this assumption will generate errors when calculate the elements in **Ps** matrix in (6). As generally the width of on-chip conductors is greater than its thickness, the accuracy of the proposed model can be is directly related to the ratio of trace spacing and their widths, as

$$r = s / \max(w_s, w_g) . \tag{47}$$

Fig. 8 shows the relative derivations between the admittance from the proposed circuit model and that from FEM. The derivations is defined as the percentage of the average difference of the curves from two different methods in the frequency range from 50 MHz to 50 GHz. The derivation is plotted versus the ratio *r* defined in (34). When the ratio of trace spacing and width is smaller than 1, the distributions charges cannot be considered as uniform on the surface of the each conductor, thus, the proposed circuit model introduces large errors. However, when the ratio is larger than 1, the derivations of both the capacitance and conductance from circuit model and FEM are less than 10%.

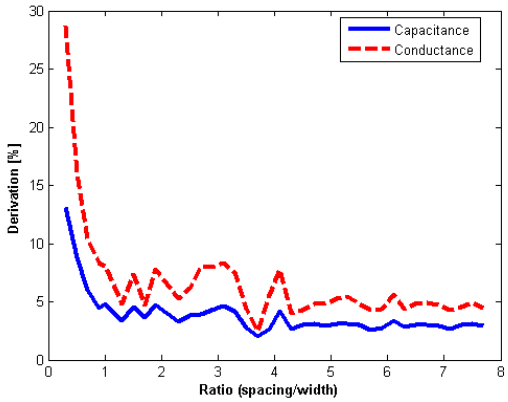


Fig. 8 Derivations of capacitance and conductance for on-chip CPW using FEM and model proposed in this paper. The x axis is the ratio of trace spacing to width defined in (34). The y axis is the average derivation in percentage from 50 MHz to 50 GHz.

Combined the circuit models for shunt admittance and series inductance, the model for per-unit-length parameters of on-chip CPW structure is shown in Fig. 9.

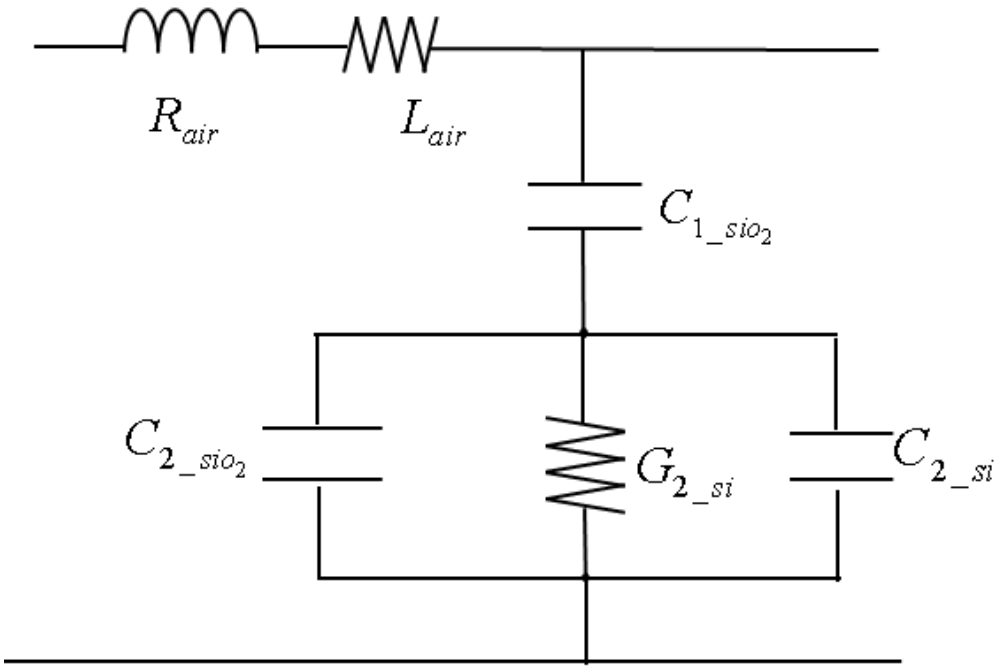


Fig. 9 Equivalent circuit model of 2-D CPW structure in Fig. 1 with per-unit-length parameters

B. Validations of the Proposed Model

First, we validate our model with simulations using high frequency structural simulator (HFSS)- a commercial full-wave simulator based on finite element method (FEM) [29]. The CPW structures under study are shown in Fig.1. The widths ws and wg of the signal and ground traces are all 10 um. The spacing between traces is also 10 um. The thickness t of the metal is 1 um. The height of the metal layer to the silicon substrate h is 0.5 um. Both S21 and S11 get good correlations, as shown in Fig. 10

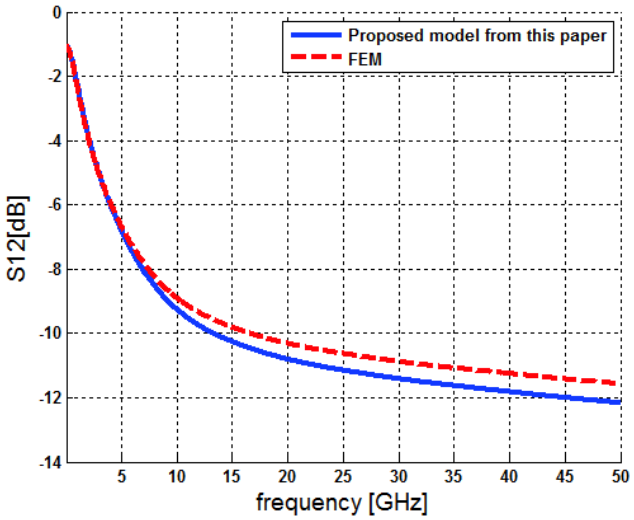


(a)

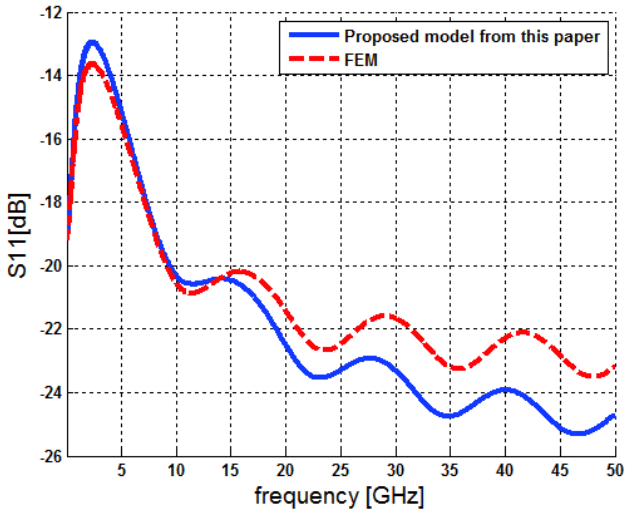


(b)

Fig.10 Comparison between S parameters using proposed model and full-wave FEM simulations for CPW geometry in Fig. 1 (a) S21 (b) S11

We also validated our model with measurements for CPW structures on a test interposer. The layout and stack up of the test interposer with CPW structures is shown in Fig. 11. The ground and signal trace widths wg and ws are all 10 um. The spacing s is 20

um. The length of the CPW is 4.8 mm. The conductivity of silicon is $10^{\Omega \cdot cm}$. GSG microprobe with 100 um pitch size was used in the measurement. To calibrate the effects of microprobe and probing pads on M2, same CPW structures with two different lengths of 0.1 mm and 2.4 mm are also designed. A hybrid calibration method introduced in [30] is used to remove the effects of the probing pads. After calibration, S parameters of 4.7 mm CPW line could be extracted, and compared with the results from the proposed model in Fig. 12. Good correlations have been achieved up to 25 GHz. The discrepancy is due to inaccuracy geometry during IC fabrication process.

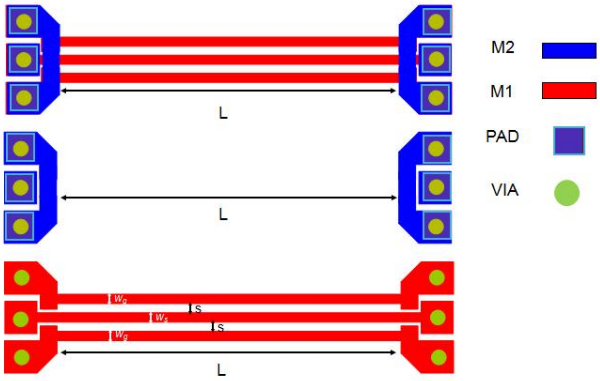


(a)

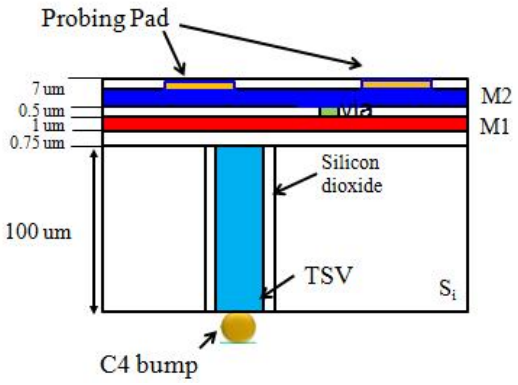


(b)

Fig. 11 CPW structure fabricated on a silicon interposer: (a) layout (b) stack up

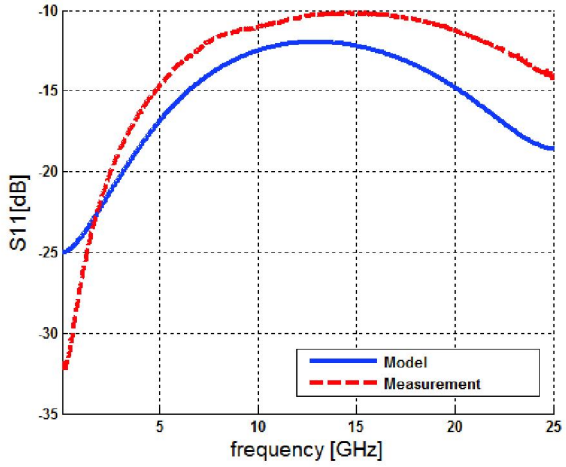


(a)

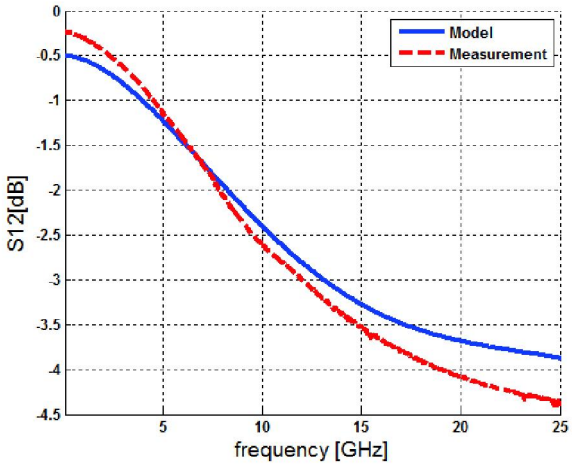


(b)

Fig.12 Comparison between S parameters using proposed model and measurement for CPW geometry in Fig. 11 (a) S11 (b) S21

## IV. CONCLUSION

In this paper, we proposed a new equivalent circuit model is proposed to model coplanar traces on silicon interposer. The 2D lossy metal-isolator-semiconductor (MIS) coplanar waveguide (CPW) is represented by simple RLGC circuit derived based on PEEC

method. The model provides physical insight and directly related to geometry. It is also demonstrated in the paper that the silicon effects on series impedance can be neglected in conventional CMOS processes. A test 2.5 silicon interposer is fabricated to validate the effectiveness of the model. The presented circuit model shows good correlations with full-wave simulations as well as the measurements on the test interposer.

## REFERENCES

[1] J.Q. Lu, "3-D Hyperintegration and Packaging Technologies for MicroNano Systems," *Proceeding of IEEE*, vol.97, no.1, pp.18-30, Jan. 2009.

[2] K.C Saraswat and F. Mohammadi, "Effect of Interconnection Scaling on Time Delay of VLSI circuits," *IEEE Trans Electron Device*, Vol 29, pp. 645-50,1982.

[3] Chai, T.C. Lau, J.H. Selvanayagam, C.S., Biswas, K. Shiguo Liu, Pinjala, D. , Tang, G.Y., Ong, Y.Y. , Vempati, S.R. , Wai, E. , Li, H.Y. , Liao, E.B. , Ranganathan, N. , Kripesh, V. , Jiangyan Sun , Doricko, J. , Vath, C.J. , "Development of through silicon via (TSV) interposer technology for large die (21×21mm) fine-pitch Cu/low-k FCBGA package," *Electronic Components and Technology Conference,* 2009*,* pp. 305-312.

[4] Lau, J.H, "Evolution, challenge, and outlook of TSV, 3D IC integration and 3D silicon integration," *2011 International Symposium on Advanced Packaging Materials (APM),* 25-28 Oct. 2011, pp. 462-488.

[5] T. Zwick, Y. Tretiakov, and D. Goren, " On-chip SiGe transmission line measurements and model verification up to 110 GHz," *IEEE Microwave and Wireless Components Letters,* , vol. 15, issue 2., pp.65-67, 2005.

[6] Kopcsay, G.V., Restle, P.J., Smith, H.H., Katopis, G., Becker, W.D., Coteus, P.W., Surovic, C.W., Rubin, B.J., Dunne, R.P., Jr., Gallo, T. , Jenkins, K.A., Terman, L.M., Dennard, R.H., Sai-Halasz, G.A., Krauter, B.L., Knebel, D, "When are transmission-line effects important for on-chip interconnections?," *IEEE Trans. Microwave Theory Tech.*, vol. 45, issue. 10, pp. 1836 - 1846, Oct. 1997.

[7] F. Bertazzi, F. Cappelluti, S. Guerrieri, F. Bonani, and G. Ghione, "Self-consistent coupled carrier transport full-wave EM analysis of semiconductor traveling-wave devices," *IEEE Trans. Microwave Theory Tech.*, vol. 54, no. 4, pp. 1611 - 1618, Jun. 2006.

[8] H. Hasegawa, M. Furukawa, and H. Yanai, "Properties of microstrip line on Si-$SiO_2$ systems," *IEEE Trans. Microwave Theory Tech*, vol. MTT-19, pp. 869–881, Nov. 1971.

[9] J. Aguilera, R. Marques, and M. Horno, "Improved quasi-static spectral domain analysis of microstrip lines on high-conductivity insulator-semiconductor substrates," *IEEE Trans. Micro Guided Wave Lett.,* vol. 9, no. 2, pp. 57 - 59, Feb. 1999.

[10]J. Kucera and R. Gutmann, "Effect of finite metallization and inhomogeneous dopings on slow-wave-mode propagation," *IEEE Trans. Microwave Theory Tech.*, vol. 45, no 10, pp. 1807-1810, Oct. 1997.

[11]G. Plaza, R. Marques and F. Medina, "Quasi-TM MoL/MoM approach for computing the transmission-line parameters of lossy lines," *IEEE Trans. Microwave Theory Tech.*, vol. 54, no 1, pp. 198–209, Jan 2006.

[12]T. Demeester and D. Zutter "Quasi-TM Transmission Line Parameters of Coupled Lossy Lines Based on the Dirichlet to Neumann Boundary Operator," *IEEE Trans. Microwave Theory Tech.,* vol. 56, no 7, July 2008.

[13]Y. Kwon, V. Hietala and K. Chamlin, "Quasi-TEM analysis of 'slow-wave' mode propagation on coplanar microstructure MIS transmission lines," *IEEE Trans. Microwave Theory Tech.*, vol. MTT-35, no 6, pp. 545–551, Jun. 1987.

[14]A. Weisshaar, H. Lan, A. Luoh, "Accurate Closed-Form Expressions for the Frequency-Dependent Line Parameters of On-Chip Interconnects on Lossy Silicon Substrate," *IEEE Trans. Advanced Packing.*, vol. 25, no 2, May. 2002.

[15]J. Zheng, Y. Hahm, V. Tripathi, and A. Weisshaar, "CAD-Oriented equivalent-circuit modeling of on-chip interconnects on lossy silicon substrate", *IEEE Trans. Microwave Theory Tech.,* vol. 48, no 9, Sep 2000.

[16]V. Milanovic, M. Ozgur, D. DeGroot, J. Jargon, M. Gaitan, M. Zaghloul, "Characterization of Broad-Band Transmission for Coplanar Waveguides on CMOS Silicon Substrates," *IEEE Trans. Microwave Theory Tech*., vol. 46, no 5, May 1998.

[17]K. Kang, L. Nan, S. Rustagi, K. Mouthaan, J. Shi, R. Kumar, W. Yin, L, Li, "A Wideband Scalable and Spice-Compatible Model for On-Chip Interconnects Up to 110 GHz," *IEEE Trans. Microwave Theory Tech*., vol. 56, no 4, April 2008.

[18]A. Ruehli, "Inductance calculation in a complex integrated circuit environment," *IBM. J. RES. Develop.,* vol. 16, pp. 470-481, Sept. 1972.

[19]R.Wu, C. Kuo and K. Chang, "Inductance and resistance computations for three-dimensional multiconductor interconnection structures," *IEEE Trans. Microwave Theory Tech.,* vol. 40, no 2, Feb 1992.

[20]L. Tiemeijer, R. Pijper, R. Havens, and O. Hubert, "Low-loss patterned ground shield interconnect transmission lines in advanced IC processes," *IEEE Trans. Microwave Theory Tech*., vol. 55, no 3, Mar. 2007.

[21]A. Sayag, D. Ritter and D. Goren, “Compact modeling and comparative analysis of silicon-chip slow-wave transmission lines with slotted bottom metal ground planes,” *IEEE Trans. Microwave Theory Tech*., vol. 57, no 4, April. 2009.

[22]J. Zheng, V. Tripathi and A. Weisshaar, “Characterization and modeling of multiple coupled on-chip interconnects on silicon substrate”, *IEEE Trans. Microwave Theory Tech*., vol. 49, PP 1733-1739, Oct. 2001.

[23]Clayton R. Paul, “Analysis of Multiconductor Transmission Lines,” John Wiley & Sons, Inc. New York, 1994, pp. 69–72.

[24]A. E. Ruehli, P. A. Brennan. “Efficient capacitance calculations for three dimensional multiconductor systems,” *IEEE Transactions on Microwave Theory and Techniques*, MTT-21(2):76–82, February 1973.

[25]Silvester, P.; , "TEM wave properties of microstrip transmission lines," *Electrical Engineers, Proceedings of the Institution of* , vol.115, no.1, pp.43-48, January 1968.

[26]G. Zhong, and C. Koh, “Exact Closed-Form Formula for Partial Mutual Inductances of Rectangular Conductors”, *IEEE Transactions on Circuits and Systems I*, Vol. 50, No. 10, Oct, 2003.

[27]W. Yao, S. Pan, B. Achkir, J. Fan and L. He, “Modeling and application of multi-port TSV network in 3D IC”, *IEEE Transactions on Computer-Aided Design of Integrated Systems*, Vol. xx, No. xx, Jan, 2012.

[28]Y. Chow, J. Yang, D. Fang, G. E. Howard, “A closed-form Spatial Green’s Function for the Thick Microstrip Substrate”, *IEEE Trans. Microwave Theory and Techniques*, Vol. 39, No 3, March 1991.

[29]HFSS, http://www.ansys.com.

# SECTION

# 2. CONCLUSION

In the first paper, previous method of deriving Green function in multi-layer media was reviewed. DCIM has been used to derive the Green function with lossy media. The study of applying the methods to the real applications of 3DIC shows at image theories can be applied to magnetic vector Green functions at low frequency, however, multiple images should be considered for electric potential Green's function. At high frequency, surface-wave term has far-field effects when the distance of the interconnect is far. Spatial-wave term becomes to dominate when the pitch size becomes larger.

In the second paper, a robust and automatic method to extract the surface-wave poles of the spectral-domain Green's functions for general layered media is proposed. Both lossless and lossy dielectric materials can be effectively handled. The proposed method can accurately identify the surface-wave poles located close to the branch cut. Through the numerical examples and the comparisons with the previously published results, the proposed approach has been demonstrated more effective and accurate to handle lossy layered media.

In the third paper, a new equivalent circuit model is proposed to model coplanar traces on silicon interposer was proposed. The 2D lossy metal-isolator-semiconductor (MIS) coplanar waveguide (CPW) is represented by simple RLGC circuit derived based on PEEC method. The model provides physical insight and directly related to geometry. It is also demonstrated in the paper that the silicon effects on series impedance can be

neglected in conventional CMOS processes. A test 2.5 silicon interposer is fabricated to validate the effectiveness of the model. The presented circuit model shows good correlations with full-wave simulations as well as the measurements on the test interposer.

# VITA

Siming Pan was born on April 8th, 1986 in Lanzhou, China. In August 2008, he obtained his Bachelor's degree from Tsinghua University in Electrical Engineering, Beijing, China. In 2010, he received the Master degree in Electrical Engineering from the Missouri University of Science and Technology. He received President's Memorial Award from IEEE Electromagnetic Compatibility Society in 2009. In August 2015, he received his Ph.D. in Electrical Engineering from Missouri University of Science and Technology.